

This Page Is Inserted by IFW Operations
and is not a part of the Official Record

BEST AVAILABLE IMAGES

Defective images within this document are accurate representations of the original documents submitted by the applicant.

Defects in the images may include (but are not limited to):

- BLACK BORDERS
- TEXT CUT OFF AT TOP, BOTTOM OR SIDES
- FADED TEXT
- ILLEGIBLE TEXT
- SKEWED/SLANTED IMAGES
- COLORED PHOTOS
- BLACK OR VERY BLACK AND WHITE DARK PHOTOS
- GRAY SCALE DOCUMENTS

IMAGES ARE BEST AVAILABLE COPY.

**As rescanning documents *will not* correct images,
please do not report the images to the
Image Problem Mailbox.**

REMARKS

This amendment is filed in response to the Office Action mailed on December 9, 2003. Claims 12-40 are pending in the instant application. Claims 1-11 were previously cancelled. Claims 39 and 40 have been added. Claims 12 and 24 have been amended. The undersigned expresses his appreciation for the courtesy of granting a personal interview with him and one of the inventors, Tibor Juhasz, on April 20, 2004. During the interview the Stern and Warner references cited in the Office Action were discussed, and the Examiner indicated that if the claims are amended to recite that a side wall is formed as the laser beam forms removable corneal layer or internal corneal tissue is accessed, the claimed subject matter would distinguish over those references. The Swinger-Lai reference was discussed in general terms and it was agreed that the applicant would discuss that reference in this response.

The following issues are outstanding in the instant application:

- The pending claims have been rejected under 35 U.S.C. § 103(a) as being allegedly obvious over Stern and Warner
- The Examiner requested in the April 20, 2004 interview that the Applicants discuss U.S. Patent No. 6,325,792 (Swinger/Lai)

I. Stern and Warner References

There two pending independent claims, claims 12 and 24. They have both been amended to recite that a sidewall is formed at an angle when the method is performed. This feature distinguishes over Warner because Warner uses a microkeratome to form a flap with a flat surface and no sidewall or anything similar to a sidewall. A flap formed by this method has the disadvantages described in the amendment filed March 4, 2003, and will not be repeated here.

Stern is completely different from Warner and there is no suggestion that the two references could be combined. The Stern article reports the results of surface ablation tests enucleated bovine eyes by using visible light that is not practical for living eyes. There is no suggestion of using any of the information in Stern to form a removable corneal layer or

accessing internal corneal tissue by any method other than with a microkeratome. Even if Stern could be combined with Warner, there is still no teaching of any type of layer or other means of access in which a sidewall is formed. Thus, even if Warner and Stern could be combined, the addition of the sidewall feature is believed to distinguish the claims over these references.

II. Swinger/Lai Reference

As for the Swinger/Lai patent, it lacks an enabling disclosure and is different from the claimed invention in the pending application because Swinger/Lai teaches that the corneal flap must be formed by cutting with minimum pulse energy. This means that pulse energies as close as possible to the breakdown must be used. In order to achieve these stated goals, Swinger/Lai limits the energy density of the pulses to below $5 \mu\text{j}/(10\mu\text{m})$.² *See*, U.S. patent 6,325,792, col. 8, lns. 33-38; col. 15, lns. 46-55; col. 25, lns. 21-22 (“. . . keeping the beam energy or irradiance to a minimum.”); claim 1, col. 36, lns. 41-42; claim 14, col. 38, lns. 12-13.

The use of minimum pulse energy is different from the claimed invention that has an optimized pulse energy density that is much greater than the minimum pulse energy taught by Swinger/Lai. This optimized pulse energy is necessary in order to achieve contiguous high quality cuts in the cornea in order to perform the claimed methods.

This optimized pulse energy is described in the subject application by reference to U.S. patent 4,988,348, which is mentioned in the specification as disclosing a procedure whereby corneal tissue is first removed to correct vision, and discloses a pulsed laser beam for photoalteration of stromal tissue. *See*, specification p. 2; MPEP, Sec. 608.01(p). The ‘348 patent teaches that for stromal tissue removal, it is important that the optimal pulse energy must be at least 10 J/cm^2 (i.e., $10 \text{ microJoule}/(10 \text{ micron})^2$). *See* col. 8, lns. 1-8.

The larger pulse energy density at the optimized pulse energy provides clean and contiguous resections in the tissue, while the minimum pulse energy density taught by Swinger/Lai provides only small and localized damage points in the tissue with their size is considerably smaller than the diameter of the focal spots.

The inadequacy of the pulse energy required in Swinger/Lai has been shown by studies described in several articles. *See*, (1) A.J. Joglekar et.al., Optics at Critical Intensity: Applications to Nanomorphing, Proceedings of the National Academy of Sciences, vol. 101, p. 5856-5861, (2004); (2) A. P. Joglekar *et al.*, A Study of the Deterministic Character of Optical Damage by Femtosecond Laser Pulses and Applications to Nanomachining, Applied Physics B, vol. 77, p. 25-30. (2003). These articles show that the size of localized damage points can be as small as few hundred nanometers, and they do not result in separable cuts in the tissue. Moreover, due to their small and gentle effect, their practical applications are in cellular microsurgery, such as cutting genes inside cells. This is in contrast to the effect of pulses above the optimized pulse energy density where the photodisruption generates cavitation bubbles that are much larger in a way that they touch each other to provide clean and contiguous macroscopic level tissue resections as it was shown by (1) Ratkay-Traub et al and Nordan et.al., First Clinical Results with the Femtosecond Neodymium-glass Laser in Refractive Surgery, Journal of Refractive Surgery, vol.19, p.94-103 (2003); (2) L Nordan *et al.*, Femtosecond Laser Flap Creation for Laser *in situ* Keratomileusis: Six month follow up of initial U.S. clinical series. Journal of Refractive Surgery, vol. 19. p.8-14, (2003). The energy density or fluence used in the surgeries described by Ratkay-Traub and Nordan is in the range of 75 to 100 J/cm², (75 to 100 microJoule/(10 micron)²) 75 to 100 J/cm², (75 to 100 microJoule/(10 micron)²), that is 15 to 20 times larger than the upper limit (5 J/cm² (5 microJoule/(10 micron)²) given by Swinger-Lai. Copies of these articles are attached.

Independent claims 12 and 24 have been amended to recite that the pulsed laser beam has an optimized pulse energy density above a minimum level for achieving tissue modification. In view of the above, each of the presently pending claims in this application is believed to be in immediate condition for allowance. Accordingly, the Examiner is respectfully requested to pass this application to issue. If there any questions, please call the undersigned at the telephone listed below.

Enclosed herewith is a check covering the RCE transmittal fee and the fee for a 3-month extension of time. Applicant believes no additional fee is due with this response. However, if a fee is due, please charge our Deposit Account No. 06-2375, under Order No. HO-P02276US1 from which the undersigned is authorized to draw.

Application No.: 09/536,861

Docket No.: HO-P02276US1

Dated: June 9, 2004

Respectfully submitted,

By

Paul E. Krieger

Registration No.: 25,886

FULBRIGHT & JAWORSKI L.L.P.

1301 McKinney, Suite 5100

Houston, Texas 77010-3095

(713) 651-5151

(713) 651-5246 (Fax)

Attorney for Applicant

Optics at critical intensity: Applications to nanomorphing

Ajit P. Joglekar*, Hsiao-hua Liu†, Edgar Meyhöfer‡, Gerard Mourou†, and Alan J. Hunt*§

*Department of Biomedical Engineering, University of Michigan, 300 North Ingalls, 972, Ann Arbor, MI 48109; †Center for Ultrafast Optical Science, University of Michigan, 2200 Bonisteel Boulevard, Ann Arbor, MI 48109; and ‡Department of Mechanical Engineering, University of Michigan, 2350 Hayward Street, Ann Arbor, MI 48109

Edited by Erich P. Ippen, Massachusetts Institute of Technology, Cambridge, MA, and approved March 1, 2004 (received for review November 13, 2003)

Laser-induced optical breakdown by femtosecond pulses is extraordinarily precise when the energy is near threshold. Despite numerous applications, the basis for this deterministic nature has not been determined. We present experiments that shed light on the basic mechanisms of light-matter interactions in this regime, which we term “optics at critical intensity.” We find that the remarkably sharp threshold for laser-induced material damage enables the structure or properties of materials to be modified with nanometer precision. Through detailed study of the minimum ablation size and the effects of polarization, we propose a fundamental framework for describing light-matter interactions in this regime. In surprising contrast to accepted damage theory, multiphoton ionization does not play a significant role. Our results also reject the use of the Keldysh parameter in predicting the role of multiphoton effects. We find that the dominant mechanism is Zener ionization followed by a combination of Zener and Zener-seeded avalanche ionization. We predict that the minimum feature size ultimately depends on the valence electron density, which is sufficiently high and uniform, to confer deterministic behavior on the damage threshold even at the nanoscale. This behavior enables nanomachining with high precision, which we demonstrate by machining highly reproducible nanometer-sized holes and grooves in dielectrics.

The invention of the laser has led to the generation of increasingly large optical electric fields, which have revealed a succession of new high-intensity optical regimes. This succession started with bound-electron nonlinear optics (1), with laser fields of strength comparable with the Coulomb field that an electron experiences near the nucleus, and has progressed through regimes of multiphoton ionization (MPI) and high harmonic generation to relativistic optics in which the most powerful lasers drive the electrons to quiver velocities close to the speed of light. Perhaps in the excitement of progress toward higher-energy regimes, one important regime has received relatively less attention: optics at critical intensity (OCI). This regime encompasses the remarkably sharp material transitions that occur when the optical field energy is very near the threshold for material breakdown through ionization of valence electrons.

A decade ago chirped-pulse amplification lasers (2) made it possible to study in detail the damage threshold as a function of pulse duration, which led to the discovery of a fundamental property of OCI: for pulses <5 ps, the damage threshold becomes deterministic and is very sharp and reproducible (within 1%), as opposed to the stochastic behavior (20–50%) for longer pulses (3). This property, combined with the lack of thermal diffusion and minimal shock waves, allows for nanomorphing: material modification with subwavelength feature size in virtually any material. This is possible only in the OCI regime; laser damage is only sufficiently precise when using subpicosecond pulses with energy just above the optical-damage threshold. OCI transports the field of laser matter interaction from the macro- and microscale to the submicrometer scale, or as demonstrated here even the nanoscale domain (<100 nm),

with important applications including cell surgery, electronics, microelectromechanical systems, and micro- and nanofluidics.

Despite the important current applications and enormous potential for new ones, the fundamental physics of OCI, particularly the deterministic character of dielectric breakdown, remains largely unresolved. To address this issue, we present a detailed study of laser damage in the subpicosecond domain. We find that, contrary to the common belief (1, 4–6), MPI does not play an important role in optical damage; the dominant optical-damage mechanism is a combination of Zener ionization (tunneling) and Zener-seeded saturation avalanche ionization. Furthermore, we find that the remarkable precision and reproducibility of the optical damage can be explained by a mechanism in which the threshold depends on uniformity of the valence electron density in the damaged material. These findings make it clear that the ultimate limits for machining with light are far beyond what was recognized previously; even ultrahigh-precision nanomachining of materials with ill-defined or variable band gaps is possible, and we demonstrate this by machining nanoscale holes and lines in a variety of materials. Furthermore, we demonstrate that ablated regions have truly precise boundaries; surrounding changes, when present, are caused by deposition of extruded material that can be entrained. These findings represent major advances for practical application of nanomorphing and the fundamental understanding that comes from rigorously establishing the physical limits of optical damage, and provide a cohesive understanding of both the incredible precision of OCI and why this precision is possible.

Laser–Matter Interaction at Critical Intensity

Focused pulses from a high-power laser can damage virtually any material when the induced electric field is high enough to produce optical breakdown. It is believed that optical breakdown in dielectric materials proceeds by avalanche ionization, in which initial (seed) unbound electrons in the target material are accelerated by the laser electric field to create a cascade of free electrons through collisions. This process occurs even in transparent materials, which become opaque light absorbers when the free-electron density is nearly equal to or greater than the critical density for the light considered. Optical breakdown shows a highly nonlinear dependence on intensity, and this allows damage to be restricted to subdiffraction limit areas by “thresholding” (Fig. 1a). This effect allows fabrication of submicrometer features (7–11), and we demonstrate that even nanoscale features can be produced with ultrahigh precision (Fig. 1 b–d and ref. 12).

For pulses longer than ≈ 10 ps, the threshold fluence for optically induced dielectric breakdown depends strongly on the pulse duration and scales with $T^{1/2}$, where T is the pulse duration

This paper was submitted directly (Track II) to the PNAS office.

Abbreviations: MPI, multiphoton ionization; OCI, optics at critical intensity; LP, linearly polarized; CP, circularly polarized.

§To whom correspondence should be addressed. E-mail: ahunt@umich.edu.

© 2004 by The National Academy of Sciences of the USA

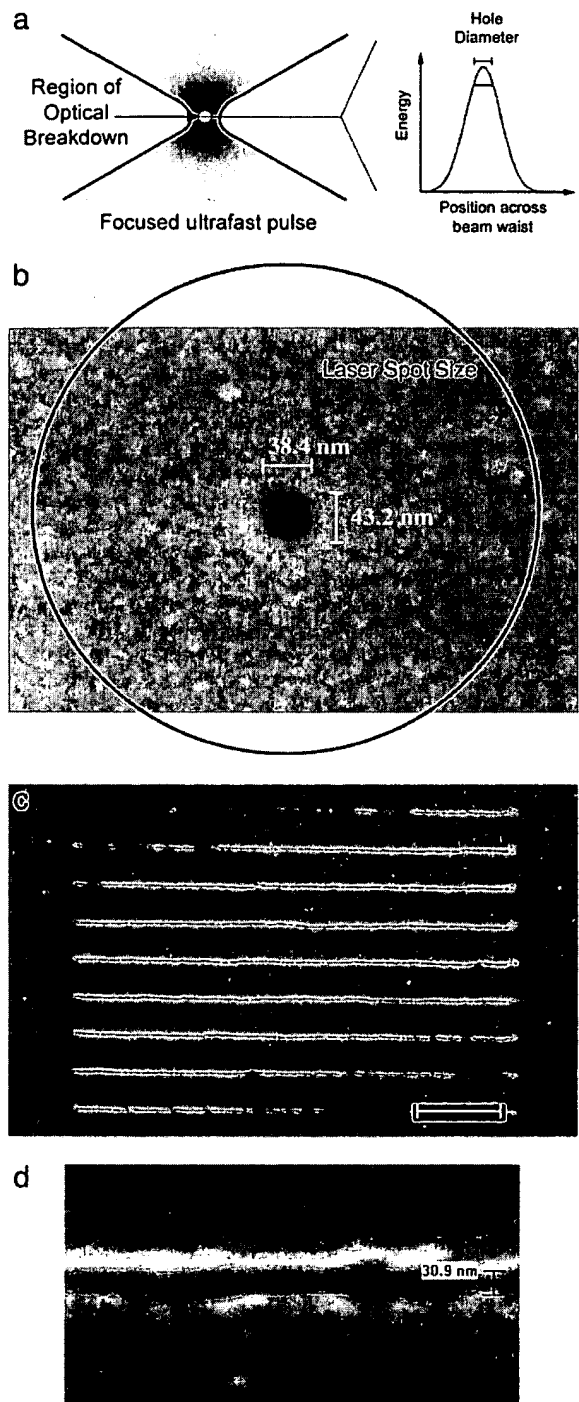


Fig. 1. (a) Illustration of how an ultrashort laser pulse can create an ablation localized to a region smaller than the light resolution limit. As the pulse energy is decreased, a smaller portion of focus spot exceeds the energy threshold for optical breakdown, thus allowing formation of subdiffraction features. (b) Example of a nanometer-scale hole. The red circle indicates the $1/e^2$ focus-spot size. Studying OCI in detail required a very stable laser. We selected a directly diode-pumped Nd:glass, chirped-pulse amplification laser system (Intralase Corp., Irvine, CA) operating at 1,053 nm, with a repetition rate of 1.5 kHz and a pulse width of 800 fs, which was focused through a high-numerical-aperture objective of an inverted microscope as described in ref. 12. (c and d) Scanning electron micrographs of \sim 30-nm-wide channels machined in glass. (Scale bar in c, 2 μ m.) A channel was produced by scanning the sample through the laser focus with the help of a piezoelectric nanostage (Mad City Labs, Madison, WI) such that the successive pulses hit the sample 50 nm apart.

(e.g., ref. 1). Bloembergen (1) advanced the theory that breakdown is based on avalanche ionization, in which seed electrons are derived from the preexisting free-electron background in case of long pulses or by MPI for short pulses. He predicted that there would be a change in the physics for optical-damage threshold as pulse widths went into the femtosecond regime and that statistical fluctuation would decrease. In 1982, Solieau and coworkers (13, 14) detected the beginning of this transition at \approx 10 ps. They found that the damage threshold was spot-size-dependent and concluded that it had an extrinsic character in which the initial electrons were provided by defects or impurities. Work at the University of Michigan confirmed the transition but also found the damage threshold to be deterministic for short pulses. This work demonstrated that the character of optical damage dramatically changes when the pulse duration is reduced below 10 ps: the pulse-duration dependence of the damage threshold becomes weak and no longer scales as $T^{1/2}$ (refs. 3 and 7). The shot-to-shot threshold variability also decreases with pulse duration, becoming increasingly deterministic. These investigators proposed that the nearly deterministic behavior was the result of a combination of two nonlinear processes: MPI seeding and saturation of the impact-ionization coefficient $\eta(E)$ at high field, as predicted for dc or low-frequency electric fields by Thorner (14). Slightly later, a similar study conducted at the Lawrence Livermore National Laboratory confirmed departure from $T^{1/2}$ scaling even for damage caused by multiple pulses. The investigators hypothesized that the plasma generation was strongly dependent on MPI and predicted a strong decrease in damage threshold for pulses well below 100 fs (5).

Although a role for MPI has been advocated consistently throughout the history of optical-breakdown research, some doubts have been expressed. Studies have failed to confirm the predicted decrease in threshold at very short pulses (5), finding instead that the damage threshold decreases only slightly or remains nearly constant to within a few J/cm^2 from 5 to 100 fs (4, 15). It has also been pointed out that frequent electron collisions in solids could strongly attenuate MPI by dephasing the electrons and the driving field (16, 17). Through a careful study of damage threshold and morphology, we conclude that MPI is not important, and in any case would not predict the phenomenally deterministic character that has allowed us to demonstrate laser machining in the nanoscale regime. We propose a theoretical framework in which OCI is dominated by a runaway process of Zener and Zener-seeded avalanche. We base this theory on five independent observations discussed below.

A Significant Role for Avalanche Ionization Is Indicated by the Relation Between Band-Gap and Quiver Energy at Threshold. For avalanche ionization to occur, the kinetic energy of a free electron must be sufficient to ionize a bound electron, i.e., of the order of the band energy gap (band gap). In the case of optically induced ionization, we expect to cross the threshold for avalanche when the band gap is of the order of the electron quiver energy, which is the time average over one light cycle of the square of the electric field average (this is expanded on in the theory section below). Because the quiver energy is proportional to intensity, a scaling of the damage threshold with the energy gap provides a strong confirmation that avalanche ionization plays an important role in breakdown in the OCI regime. We find that, for a wide range of band gaps, composition, and structures, the threshold energy, which is proportional to intensity and thus the electron quiver energy, scales with the band gap (Fig. 2), supporting the role of

¹Soileau, M. J., Williams, W. E., Van Stryland, E., Boggess, T. F. & Smirl, A. L., The 12th Annual Symposium on Laser-Induced Damage to Optical Materials, November 16–17, 1982, Boulder, CO, p. 387 (abstr.).

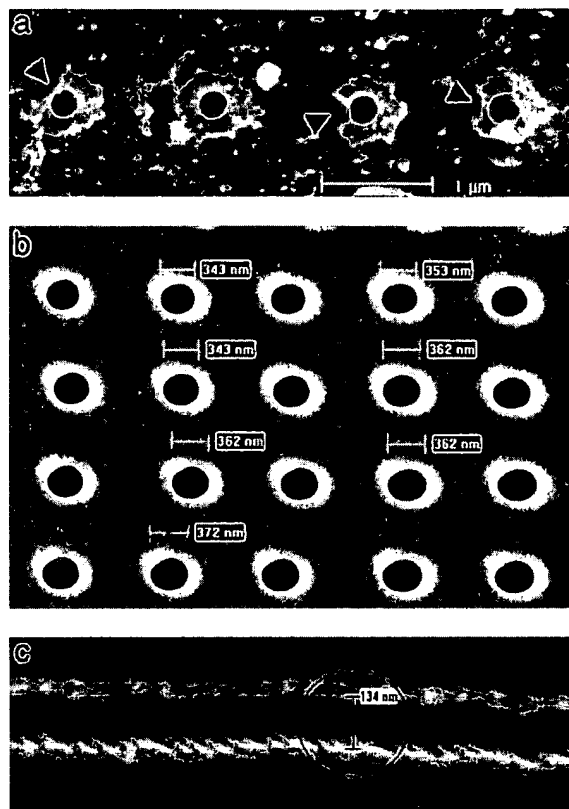
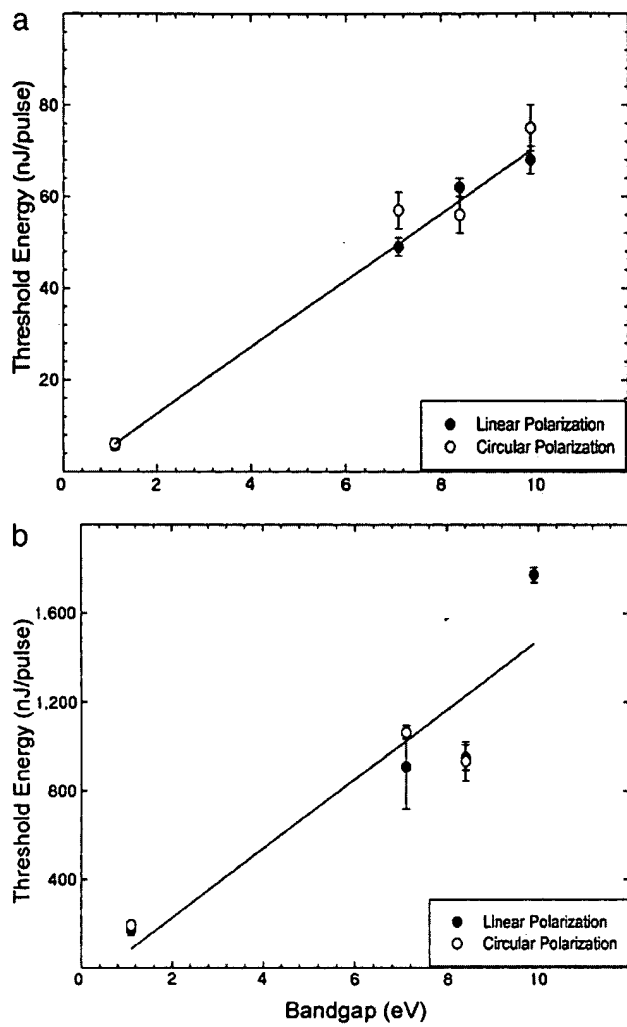


Fig. 3. Surrounding features are redeposited material extruded from the ablated region. (a) Scanning electron micrograph (SEM) of a row of holes in glass. Before viewing, the sample was blasted with pressurized gas, causing pieces of the surrounding feature to break off, revealing a flat surface below (arrowheads). (b) SEM of an array of holes in glass produced at a glass–water interface. Note that features surrounding the holes are suppressed or absent. (c) SEM of a groove machined at a glass–water interface by scanning the sample through the laser focus so that the successive pulses hit the sample 50 nm apart. Note fluting on the edges of the walls, indicating extraordinary discrimination of the damage produced by each pulse. The circle indicates the $1/4^2$ focus-spot size of the beam. The effective machining diameter of the beam thus can be made much smaller than the diffraction-limited diameter of the beam.

avalanche ionization in breakdown. This observation extends, but remains consistent with, other studies (5, 18). Surprisingly, we find that the relation holds even for silicon, in which a single photon is sufficient to ionize an electron, supporting an important role for avalanche even in a material that is easily ionized by the incident light. Note that the threshold in quartz is similar to the threshold in fused silica. Because quartz has a smaller number of extended states than fused silica, this suggests that in large band gap materials, the seed electrons are not produced by single-photon ionization due to the extended states covering the whole band gap.

The Initial Free-Electron Density Required for Avalanche Can Be Deduced from Feature Size and Morphology. The scale of the sharpness of the holes produced by optical breakdown allows us to estimate the ionized electron density preceding the onset of avalanche ionization. Initiation of avalanche requires ionized seed electrons, the density of which is multiplied on the order of 10 by the series of ionizing collisions. Because the distance

between collisions is equal to the ion average distance (≈ 0.5 nm), there must be an upper bound for the avalanche volume initiated from a single-seed electron. This volume will determine the smallest feature size.

By reducing the pulse energy to a value slightly above the threshold for material damage, we consistently machined circular holes much smaller than 100 nm (e.g., Fig. 1b). Even at these minute scales the holes have sharply delineated boundaries; the edges are smooth to the resolution of the scanning electron microscope (≈ 4 nm), which suggests that even smaller scales could be achieved by using shorter wavelengths and/or approaching closer to threshold. By spacing subsequent laser shots to produce a line of slightly overlapping holes, we found that we also could machine channels (Fig. 1c and d). This finding, in addition to further demonstrating the utility of OCI for nanoscale machining, reinforces the deterministic character of OCI: if any damage is produced in the region beyond the sharp borders of an ablation, it is so minimal that it does not affect the ablation induced by a subsequent shot. Holes often were accompanied by surrounding features, usually a raised region immediately around the holes (e.g., Fig. 3a). These raised regions sometimes broke off to reveal a flat surface below, suggesting

that they are formed by deposition of material extruded from the central hole. In support of this theory, the surrounding features were strongly attenuated when machining was performed at a surface–water interface (Fig. 3b).

From the small size and sharp edges of the holes, we can conclude that the free-electron density before avalanche starts must be at least $10^{18}/\text{cm}^3$ to ensure one electron in a volume 4 nm across (the upper limit of the roughness of the edges of the holes). This is a very high electron density, especially for large band-gap materials [e.g., 10 eV in sapphire ($1 \text{ eV} = 1.602 \times 10^{-19} \text{ J}$)]. It is far too high to be preexisting (1) and definitively demonstrates the widely held view that free electrons are produced before the onset of avalanche by MPI or band-gap (Zener) tunneling of electrons through the atomic field potential barrier, which is suppressed by the strong electric field of the intense light (19).

To Differentiate Between MPI and Zener Tunneling of Electrons, We Studied the Damage Threshold as a Function of Polarization. In contrast to MPI, the efficiency of Zener tunneling is expected to be similar for linearly polarized (LP) and circularly polarized (CP) light (20–24). We note that in gasses, theories variably predict modest reduction of the efficiency of Zener tunneling for CP versus LP light (22–24). Experimentally, the threshold for CP light was found to be ≈ 2 -fold higher (22). However, as discussed below, we do not observe this in solids. Therefore, if MPI plays a significant role, the threshold for breakdown should be significantly different for LP and CP light, which has been demonstrated in gasses in which LP and CP light have quite different ionization rates; LP light is much more efficient, especially for fourth- or higher-order photon absorption (17). This is not surprising: CP light is expected to be inefficient for inducing MPI because of dephasing caused by rotation of the driving field. In large band-gap materials such as quartz or sapphire, the predicted rate of MPI is ≈ 3 orders of magnitude less for CP compared with LP light (21, 25, 26). But theories incorporating MPI (5, 18, 27, 28) may be inappropriate in solids, for which there is the possibility of collisions between electrons on neighboring atoms. When the electron excursions become larger than the atomic distance, frequent collisions will dephase an electron and the driving field, suppressing multiphoton effects (21). Indeed an initial study by Du *et al.* (16) examined the breakdown threshold as indicated by increased light absorption by the target material and could not detect to within 10% a threshold difference between CP and LP light. Using the method of Joglekar *et al.* (12), we examined the damage threshold polarization dependence with high precision and found no dependence within 1% accuracy (Fig. 2). No polarization effects were detected for materials over a wide range of band gaps, composition, and structure at two different laser wavelengths. These results reject the commonly accepted theory that attributes MPI as a principal free-electron-generation mechanism. Likewise, our results reject application of Keldysh theory (28) to predict MPI in solids; we find threshold to be independent of polarization for Keldysh parameter γ ranging from 0.46 (glass, 1,053 nm) to 3.4 (sapphire, 527 nm), spanning both sides of $\gamma = 1.5$, the predicted boundary between domination of MPI and tunneling effects (e.g., refs. 18 and 27).

Sharp Features in Materials with Variable Band Gap Show That the Onset of Avalanche Is Not in Itself Sufficient for Breakdown. The band-gap energy may vary quite significantly from atom to atom in a given material. This is particularly true in glass, in which the band gap is highly variable, especially at the surface. This variability is not reflected in the threshold energy (Fig. 3), because on the scale of the illuminated spot the average band-gap structure varies little from one location to another. This is true even for a heterogeneous material with an ill-defined band

gap such as Corning 211 glass. However, as finer details of damage are examined, we might expect heterogeneities reflecting disparity in the threshold intensity required for the quiver energy to exceed a variable band gap. In particular, the edges of holes should be rough, and their size should be variable. On the contrary, we find that the variability of the band-gap structure is not reflected in the features, which are both sharp and repeatable even across large distances and even in Corning 211 glass (Figs. 1 and 3). From this finding we conclude that, although there is a critical intensity required for breakdown, it does not solely define the onset of damage. We propose that the sharp breakdown threshold is also defined by a critical pulse energy or fluence, which depends only on the valence electron density. Sharp, repeatable machining is then possible, because the valence electron density is expected to be homogenous across large distances, even down to the nanometer scale for good-optical-quality materials. Once the avalanche starts, it self-terminates when all valence electrons are ionized. This provides a discrete endpoint, which is necessary for deterministic behavior, as discussed below.

The Depth of Features Indicates That Damage Occurs When All Valence Electrons Are Ionized. Because thermal diffusion is extremely limited during subpicosecond pulses, optical breakdown is induced on a surface facing the laser only where sufficient light is absorbed to exceed threshold. Thus, the depth of the damage provides a measure of laser penetration during dielectric breakdown, provided that the damage is limited to depths less than the length of the beam waist. Near threshold, this depth will be of the order of the depth required for an e -fold reduction in light intensity, which for an otherwise optically transparent material corresponds to the skin depth that an electric field penetrates in the conducting ionized region. To measure the depth of ablation features, larger holes were produced in glass by focusing near-threshold energy pulses at 1,053 nm with a weakly focusing objective (0.65 numerical aperture). The depth of such holes (0.5 μm in diameter) was measured to be 50 nm with atomic force microscopy. Similar results have been observed by others (9, 12, 29). This depth is on the order of 30 nm, the skin depth corresponding to ionization of all $\approx 10^{23}/\text{cm}^3$ valence electrons, and we conclude that all valence electrons are ionized at breakdown.

A Mechanistic Explanation for the Deterministic Character of OCI

The events that lead to optical breakdown begin with the formation of a large number of charge carriers by Zener tunneling in a volume confocal with the laser at or near the surface. Although the probability of tunneling (19) is small before the threshold for avalanche is crossed, the valence electron density is large ($10^{23}/\text{cm}^3$), which leads to a significant number of free electrons tunneling to the conduction band. When the carrier quiver energy given by

$$E_{\text{osc}} = \left\langle \frac{e^2 E^2}{2m\omega^2} \right\rangle \text{ or } E_{\text{osc}} = 9.310^{-14} I \lambda^2 \quad [1]$$

becomes greater than the band gap, bonds can be broken and carriers are multiplied further by avalanche ionization. Here E_{osc} is in eV, the intensity I is in W/cm^2 , wavelength λ is in μm , E is the laser electric field in V/cm , ω is the angular frequency of the laser, m is the rest mass of an electron, and e is the charge of the electron. At the onset of avalanche, the carrier density is $\approx 10^{18}/\text{cm}^3$, as indicated by the nanoscale-feature size and sharpness. The time between collisions τ decreases as the electron energy increases to become of the order of 100 asec for eV quiver energy. The increase in free-electron density sharply augments the plasma frequency ω_p and will decrease the dielec-

tric constant to near zero when the plasma frequency reaches the laser frequency.

$$\varepsilon = 1 - \left(\frac{\omega_p}{\omega} \right)^2 \text{ with } \omega_p^2 = \frac{4\pi ne^2}{m} \quad [2]$$

The electric field in the plasma is equal to $E/\varepsilon^{1/4}$ (30). Thus, when the plasma frequency becomes close to the laser frequency ω , the electric field experiences a strong enhancement, further increasing impact ionization and producing a run-away process that will stop when all the valence electrons are ionized. When the plasma frequency becomes greater than the laser frequency ($\omega_p > \omega$), the electric field in the plasma drops, and the plasma becomes strongly absorbing. The light won't propagate and will be absorbed over the skin depth δ given by (30)

$$\frac{c}{\omega_p} < \delta < \frac{c}{\omega_p(2\omega\tau)^{1/2}} \quad [3]$$

For free-electron density of $10^{23}/\text{cm}^3$, this skin depth is of the order of 30 nm, which is comparable with the impact depth of 50 nm measured by atomic force microscopy. Fig. 4 schematically illustrates distribution of these events across the laser focus (*a*) and over time (*b*).

In the absorbing volume, the material exhibits a metallic character and the interaction is overcritical, with a low plasma temperature of several eV set by the bond breaking energy. Because the overcritical spot area is completely metallic, the situation becomes analogous to the interaction with metals in which subwavelength damage has been demonstrated (9). After a few picoseconds, the electrons will transfer their kinetics energy to the ions. Once the ions' kinetic energy is such that their displacement corresponds to a fraction of the lattice constant, the dielectric undertakes a phase transition to melt and then vaporize.

Discussion

We present a thorough characterization of OCI across materials, scales, light polarities, and wavelengths, which precipitates a physical theory for optical breakdown in solids. These fundamental findings illuminate a regime of ultrahigh-precision laser machining that enables a revolutionary approach for manufacturing nanotechnology. In contrast to previous work (13, 11), we find that damage is intrinsic in nature, without a strong local dependence on impurities or defect states within the material. We find that the deterministic character of OCI originates from Zener-seeded self-terminated avalanche ionization and does not appreciably depend on MPI.

These findings explain why laser machining using OCI is ultrahigh-precision, capable of creating features ranging from micrometers to the low end of the nanometer scale. The sharp boundaries of breakdown at OCI make it a simple matter to form more complicated structures by repeatedly machining holes at different locations such that successive features overlap (e.g., Fig. 1 *c* and *d*). Because OCI is governed by the valence electron density, it can work with any material with a uniform valence electron density (e.g., optical-quality materials), and for many applications it is simpler and more reliable compared with other methods capable of producing nanometer features (e.g., electron-beam lithography and nanoimprinting). Because all valence electrons are ionized in the region of material damage, the smallest achievable scale will ultimately be limited by the skin depth and/or the diffusion of ionized electrons out of the region of breakdown. The latter limit can be estimated at ≈ 10 nm, and because it depends on the pulse length, even smaller features might be attained by using shorter pulses. The physics of OCI are extremely well suited for a broad range of applications requiring discrete high-precision material modification, such as microelec-

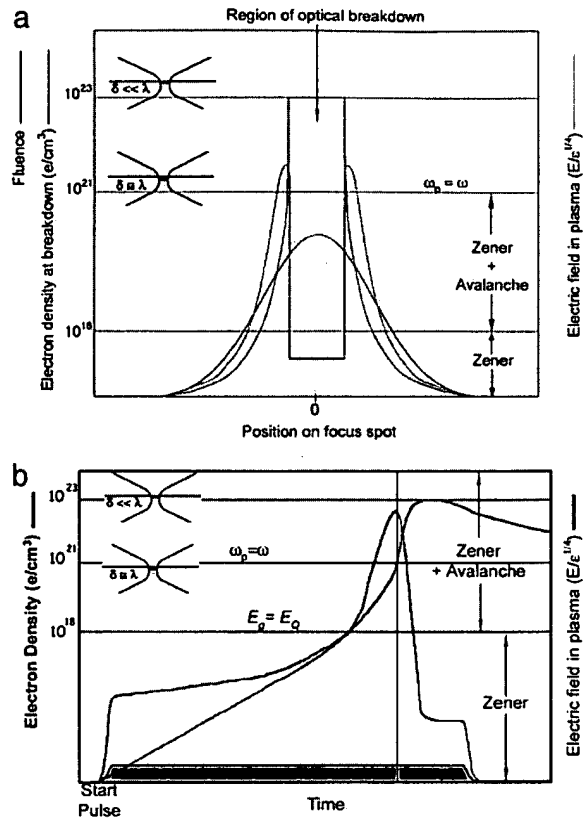


Fig. 4. (a) Schematic illustration of the distribution of processes across the laser focus, within the Rayleigh range, during material ablation. The electron density is indicated on the left axis and by the blue line. The black line indicates the profile of fluence across the Gaussian focus spot. The electric field at the onset of material damage (breakdown) is indicated by the red line. The fluence and the electric field lines indicate relative changes; actual values are not given. (Insets) Graphical illustration of the decreasing skin depth (δ) that the laser penetrates as the free-electron density increases (the speckles indicate free electrons in the dielectric). The skin depth becomes approximately equal to the incident wavelength (λ) at 10^{21} electrons per cm^3 , as illustrated (Lower Inset). The plasma frequency ω_p increases with the free-electron density. As ω_p approaches the laser frequency, the electric field experiences a strong enhancement and all valence electrons are ionized rapidly. This transition causes the material to become heavily absorbing over a skin depth that is much smaller than the wavelength, as indicated (Upper Inset), and the electric field in the plasma drops. Due to heavy absorption, the material over the skin depth is vaporized. (b) Schematic illustration of the processes that lead up to material ablation over the interval of a laser pulse. The pink region at the bottom indicates the duration of the laser pulse. The electron density is indicated on the left axis and by the blue line. The changing electric field in the region of ionization (plasma) is indicated by the red line. When the field is such that the electron quiver energy is below the band gap ($E_Q < E_g$), free electrons are produced only by Zener ionization. When the electron density passes $\approx 10^{18}/\text{cm}^3$, the quiver energy exceeds the band gap, and avalanche ionization begins. This process takes place over the skin depth (δ) that decreases as the electron density increases, becoming approximately equal to the incident wavelength (λ) at 10^{21} electrons per cm^3 , as illustrated (Lower Inset). As the plasma frequency ω_p approaches the laser frequency, the electric field experiences a strong enhancement and all valence electrons are ionized rapidly. This transition causes the material to become heavily absorbing over a skin depth that is much smaller than the wavelength (λ), as indicated (Upper Inset), and it is vaporized.

tromechanical systems construction and design, ultrahigh-density microelectronics, nanofluidics, materials science, optical memory, creation of structures to interface with cells and biological molecules, and targeted disruption of intracellular structures (e.g., refs. 12 and 31).

We acknowledge and thank Dr. Tibor Juhasz and IntraLase Corp. for making available the femtosecond laser source used in this work. We thank Dr. Jaspreet Singh for discussions regarding avalanche ionization and its importance to Zener diodes. We also thank Dr. Greg Spooner for initiating

the work that led to the present study. This work was supported by grants from the National Science Foundation and the Burroughs Wellcome Fund (to A.J.H.) and by National Science Foundation Grant Phy 0114336 and Army Research Office Grant DAAD19-03-1-0287 (to G.M.).

1. Bloembergen, N. (1974) *IEEE J. Quantum Electron.* **QE-10**, 375–386.
2. Squier, J., Salin, F., Mourou, G. & Her, H. H. (1991) *Opt. Lett.* **16**, 324–327.
3. Du, D., Liu, X., Korn, G., Squier, J. & Mourou, G. (1994) *Appl. Phys. Lett.* **64**, 3071–3073.
4. Lenzner, M., Kruger, S., Sartania, S., Cheng, Z., Spielmann, C., Mourou, G., Kautek, W. & Krausz, F. (1998) *Phys. Rev. Lett.* **80**, 4076–4079.
5. Stuart, B., Feit, M., Rubenchik, A., Shore, B. & Perry, M. (1995) *Phys. Rev. Lett.* **74**, 2248–2251.
6. Tien, A., Backus, S., Kapteyn, H., Murnane, M. & Mourou, G. (1999) *Phys. Rev. Lett.* **82**, 3883–3886.
7. Du, D., Squier, J., Kurtz, R., Elner, V., Liu, X., Gutmann, G. & Mourou, G. (1995) in *Ultrafast Phenomena IX*, ed. Barbara, P. F. (Springer, New York), p. 254.
8. Liu, X., Du, D. & Mourou, G. (1997) *IEEE J. Quantum Electron.* **33**, 1706–1716.
9. Pronko, P., Dutta, S., Squier, J., Rudd, J., Du, D. & Mourou, G. (1995) *Opt. Commun.* **114**, 106–110.
10. Schaffer, C., Brodeur, A., Garcia, J. & Mazur, E. (2001) *Opt. Lett.* **26**, 93–95.
11. Venkatakrishnan, K., Tran, B., Stanley, P. & Sivakumar, N. (2002) *J. Appl. Phys.* **92**, 1604–1607.
12. Joglekar, A. P., Liu, H., Spooner, G., Meyhofer, E., Mourou, G. & Hunt, A. J. (2003) *Appl. Phys. B* **77**, 25–30.
13. Van Stryland, E., Soileau, M. J., Smirl, A. L. & Williams, W. E. (1981) *Phys. Rev. B Condens. Matter* **23**, 2144–2151.
14. Thornber, K. K. (1981) *J. Appl. Phys.* **52**, 279–290.
15. Tien, A. (1999) Doctoral dissertation (Univ. of Michigan, Ann Arbor).
16. Du, D., Liu, X. & Mourou, G. (1996) *Appl. Phys. B* **63**, 617–621.
17. Lompré, L., Mainfray, G., Manus, C. & Thebault, J. (1977) *Phys. Rev. A At. Mol. Opt. Phys.* **15**, 1604–1612.
18. Schaffer, C. B., Brodeur, A. & Mazur, E. (2001) *Meas. Sci. Technol.* **12**, 1784–1794.
19. Sze, S. M. (1981) *Physics of Semiconductor Devices* (Wiley, New York).
20. Ammosov, M. V., Delone, N. B. & Krainov, V. P. (1987) *Sov. Phys. JETP* **64**, 1191–1194.
21. Du, D. (1996) Doctoral dissertation (Univ. of Michigan, Ann Arbor).
22. Fittinghoff, D. N., Bolton, P. R., Chang, B. & Kulander, K. C. (1994) *Phys. Rev. A At. Mol. Opt. Phys.* **49**, 2174–2177.
23. Lerner, P. B., LaGattuta, K. & Cohen, J. S. (1994) *Phys. Rev. A At. Mol. Opt. Phys.* **49**, R12–R15.
24. Lerner, P. B., LaGattuta, K. & Cohen, J. S. (1996) *J. Opt. Soc. Am. B* **13**, 96–100.
25. Gauntier, Y. & Trahin, M. (1973) *Phys. Rev. A At. Mol. Opt. Phys.* **7**, 2069–2073.
26. Reiss, H. R. (1980) *Phys. Rev. A At. Mol. Opt. Phys.* **22**, 1786–1813.
27. Kaiser, A., Rethfeld, B., Vicanek, M. & Simon, G. (2000) *Phys. Rev. B Condens. Matter* **61**, 11437–11450.
28. Keldysh, L. (1965) *Sov. Phys. JETP* **20**, 1307–1314.
29. Glezer, E. & Mazur, E. (1997) *Appl. Phys. Lett.* **71**, 882–884.
30. Eliezer, S. (2002) *The Interaction of High-Power Lasers with Plasmas* (Institute of Plasma Physics, Philadelphia).
31. Tirlapur, U. K. & Konig, K. (2002) *Nature* **418**, 290–291.

A.P. JOGLEKAR¹
 H. LIU²
 G.J. SPOONER²
 E. MEYHÖFER³
 G. MOUROU²
 A.J. HUNT⁴✉

A study of the deterministic character of optical damage by femtosecond laser pulses and applications to nanomachining

¹ 300, N. Ingalls, 952, Ann Arbor, MI 48109, USA

² 2200, Bonisteel Blvd., IST, Ann Arbor, MI 48109-2099, USA

³ 3130 GG Brown Lab/2125, Ann Arbor, MI 48109, USA

⁴ 2131 Gerstacker, 2200 Bonisteel Blvd., Ann Arbor, MI 48109, USA

Received: 28 April 2003 / Revised version: 5 June 2003
 Published online: 30 July 2003 • © Springer-Verlag 2003

ABSTRACT A remarkable feature of material damage induced by short-pulsed lasers is that the energy threshold becomes deterministic for sub-picosecond pulses. This effect, coupled with the advent of kHz and higher repetition rate chirped pulse amplification systems, has opened the field of femtosecond machining. Yet the mechanism of optical breakdown remains unclear. By examining the damage threshold as a function of polarization, we find that, contrary to established belief, multiphoton ionization plays an insignificant role in optical breakdown. The polarization independence, combined with the observed precise and uniform dielectric breakdown threshold even for nanometer-scale features, leads us to conclude that the fundamental mechanism is ‘self-terminated’ Zener-impact ionization, and that the deterministic and uniform damage threshold throughout the sample threshold stems from the uniform valence-electron density found in good-quality optical materials. By systematically exploring optical breakdown near threshold, we find that we can consistently machine features as small as 20 nm, demonstrating great promise for applications ranging from Micro ElectroMechanical Systems (MEMS) construction and microelectronics, to targeted disruption of cellular structures and genetic material.

PACS 32.80.Rm; 77.22.Jp; 81.16.-c

required intensity (Fig. 1a). This ‘thresholding’ effect is especially effective for sub-picosecond pulses, and has been applied to fabricate micrometer [1–7] and sub-micron features as small as 300 nm [4, 8–10]. Sub-picosecond lasers have also been used to make micrometer-sized holes in biological tissue for eye surgery [8], and slices across chromosomes that are micrometers long, and as thin as 100 nm [11]. We present methodology for more than an order of magnitude further reduction in feature size in hard materials, a milestone achievement that moves laser machining into the nanoscale regime.

The dynamics of optically induced dielectric breakdown depend strongly on the pulse duration. This has been most comprehensively studied by the Bloembergen group (e.g. [12]), which observed that for laser-pulse durations down to 10 ps the damage-threshold fluence scales with $T^{1/2}$, where T is the pulse duration. This group advanced the theory that breakdown is based on avalanche ionization, in which initial (seed) unbound electrons in the target material are accelerated by the extreme electric field of a short laser pulse to create a cascade of free electrons through collisions. They proposed that seed electrons are derived from the pre-existing free-electron background in the case of long pulses, or by multiphoton ionization (MPI) for short pulses. With the introduction of high-repetition-rate chirped pulse amplification (CPA) lasers [13], it became possible to continuously vary the pulse duration, allowing more precise examination of the influence of the pulse duration on the damage threshold. Initial work showed that as the pulse length drops below 10 ps: (a) the fluence threshold flattens, diverging from the $T^{1/2}$ scaling law, and (b) the shot-to-shot variability in damage is strongly attenuated. That is, the damage threshold changes from stochastic for long pulses to deterministic for short pulses [1]. To explain this deterministic behavior, a mechanism of multiphoton-seeded avalanche ionization was invoked, where in the high-field, short-pulse regime the avalanche experiences a strong saturation as predicted by Thornber [14]. Subsequent studies qualitatively confirmed the departure from the $T^{1/2}$ relation and the deterministic nature of the damage threshold for multiple [7, 15] or single [16] short-pulse shots. Again the findings were explained in terms of multiphoton-seeded avalanche. In the present study we show that, contrary to past assumptions, MPI does not play a significant role in optical breakdown. This also confirms the hypothesis that frequent electron collisions in solids strongly

1 Introduction

A principal challenge facing nanotechnology is consistently producing well-defined features much smaller than the wavelength of visible light. One approach to achieve this is to use optical breakdown, a process through which localized plasma is generated when matter is subjected to focused high-power laser pulses. This is particularly effective using very short pulses since, as the pulse duration decreases below a picosecond, the damage threshold shifts from stochastic to deterministic [1]. This highly non-linear dependence of optical breakdown on intensity allows the process to be limited to regions smaller than the spot size of the focused laser; the laser power can be selected so that only a small section of the Gaussian diffraction-limited focus exceeds the

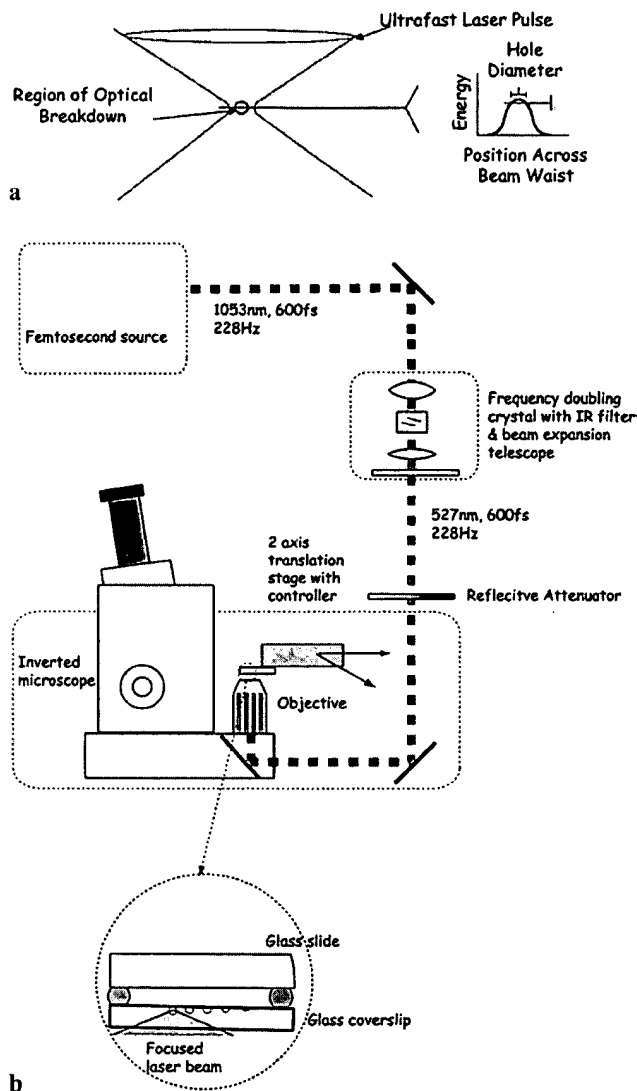


FIGURE 1 a Illustration of how an ultra-short laser pulse can create an ablation localized to a region smaller than the light-resolution limit. As the pulse energy is decreased, a smaller portion of the focal spot exceeds the energy threshold for optical breakdown, allowing formation of sub-diffraction features. b Experimental set-up for nanoscale machining

attenuate MPI by dephasing the electrons and the driving field [17, 18].

Although high-precision applications of ultra-short pulsed lasers rely on the remarkable deterministic character of femtosecond ablation, the precision of this effect has not been thoroughly assessed. In this paper we find that the damage threshold is far more deterministic than previously realized, as demonstrated by our extension of laser machining into the nanometer regime. This allows the size of ablations to be reduced to less than 20 nm, enabling a wide range of ultra-high-precision nanoscale machining applications.

2 Methods

The experiments were performed with a directly diode-pumped Nd:glass, CPA laser system (Intralase Corp., Irvine, CA) operating at 1053 nm, with 30-mW average power

at a repetition rate of 1522 Hz and a pulse width of 600 fs. The laser beam (at 1053 nm or frequency doubled with a KTP, type I crystal (Cleveland Crystals, Highland Heights, OH)) with an ellipticity of $\sim 3:1$ was expanded so that the minor axis overfilled the back aperture of the focusing objective lens. It was then brought into the epifluorescence path of an inverted microscope (Axiovert 200, Carl Zeiss Inc., Thornwood, NY) and focused by one of the two objectives: Zeiss Neofluar 1.3 NA, 100 \times objective or 0.65 NA, 40 \times (Fig. 1b). The laser was focused onto target materials, in the form of cover slips: Corning 0211 glass, single-crystal quartz (Ted Pella, Redding, CA), silicon (provided by Dr. Stephen Yalisove), and fused silica. The surface of each cover slip was cleaned with an air duster prior to machining. The cover slip was then mounted on a glass slide using double-sided tape. With the 1.3 NA oil-immersion objective, the laser beam was focused on the surface distal to the objective to avoid the oil-glass/quartz interface. With the 0.65 NA air objective, machining was carried out on the surface immediately facing the objective. Since with the 1.3 NA objective the exact location of the laser focus with respect to the cover-slip surface could not be determined with accuracy better than ~ 1 micron (by simultaneously imaging the surface), the cover slip was mounted at a known angle with respect to the beam axis. The slide was secured to a computer-controlled, two-axis motorized stage (Siskiyou Designs, Grants Pass, OR) fastened to the microscope stage. The repetition rate of the laser and the speed of the stage were adjusted to get a reasonable separation between adjoining features. As the cover slip was scanned through the fixed laser focus, the focus spot gradually descended into the surface of the material. The first visible damage to the surface (as seen with a scanning electron microscope (SEM)) at the start of a line of holes was taken as the first point of contact between the cover-slip surface and the focus spot. The feature-size measurements were done in the middle of the line. This ensured that the feature size could be studied solely as a function of pulse energy; the position of the focus with respect to the surface is maintained for different energies. The average power of the beam was measured before striking the dichroic mirror used to reflect the beam into the back aperture of the objective, and was changed by means of a reflective variable-density filter.

Samples were coated after laser machining with either gold or palladium to a thickness of $\sim 10\text{--}20$ nm in a sputter coater in preparation for scanning electron microscopy. Scanning electron microscope analysis was done on a Philips XL30 FEG microscope. Size measurements were carried out manually with an in-built function in the microscope control software.

3 Results

Figure 2a shows a typical row of holes created in the surface of Corning 0211 glass by single femtosecond pulses at 527-nm wavelength having an average pulse energy of 7.5 nJ, and focused by a 1.3 NA objective on the distal side of the cover slip. The features are striking in their reproducibility, and they are identical in size within the measurement error of the SEM ($\sim 10\%$). This is all the more surprising in a heterogeneous material such as glass, in which the band

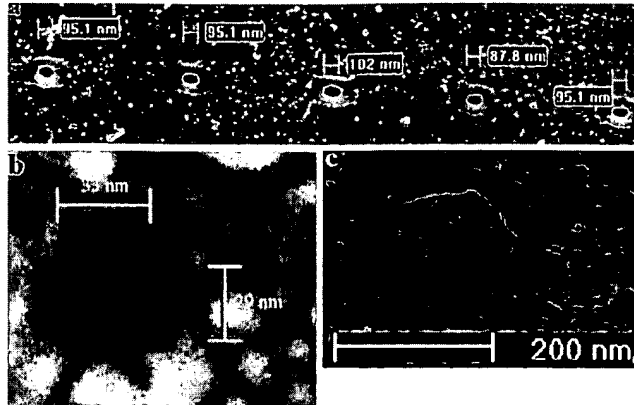


FIGURE 2 a Scanning electron micrograph (SEM) of a row of holes in Corning 0211 glass. b, c Examples of nanometer-scale holes. The hole in c is 15 nm in diameter

gap varies considerably from spot to spot. The features frequently exhibit a raised region immediately around the central hole (e.g. Fig. 2a). Occasionally, a flat substrate is revealed below portions of the surrounding raised region that have apparently broken off (not shown). This suggests that raised areas are formed by deposition of material extruded from the holes. The size of the central hole and the surrounding features depends strongly upon average pulse energy, as well as the relative position of the laser focal spot with respect to the material surface. The smallest holes were found near the beginning of a line, where the laser focus just made contact with the surface of the cover slip. By reducing the pulse energy to a value slightly above the threshold at which features vanish (~ 4 nJ), we consistently machined circular holes as small as 20 nm (e.g. Fig. 2b, c). In some cases holes as small as 15 nm were produced at higher energies at the beginning of a line where the focus first encountered the surface (Fig. 2c). Even at these minute scales, the holes have sharply delineated edges (< 4 nm, below the resolution limit of the SEM), suggesting that even smaller scales might be achieved using shorter wavelengths and/or approaching still closer to threshold. The displacement in the z axis from end to end of a row of holes machined across a tilted cover slip was about the same as the largest hole diameters, indicating that they were created when a roughly spherical region at the laser focus encountered the surface of the target (Fig. 3).

The deterministic breakdown threshold and the Gaussian intensity profile of a laser pulse imply an exponential dependence of the size of the breakdown zone on the pulse energy. We systematically studied this dependence at 1053- and 527-nm wavelengths in a variety of materials (Table 1). We measured the diameters for central holes (hole diameter) as well as the surrounding features (feature diameter). The results for the Corning 0211 glass for the wavelength of 1053 nm with two objectives are shown in Fig. 4. Assuming that the size reflects thresholding of the Gaussian intensity profile of the focused spot (see Fig. 1a), we fit the hole and the surrounding feature-size data to $D = \sigma \sqrt{8 \ln(E/\gamma)}$, where D is the diameter, E is the pulse energy, and γ and σ are fitting parameters: γ gives the threshold energy. The threshold energy appears different for the holes and the surrounding features when using the higher NA (NA = 1.3) objective

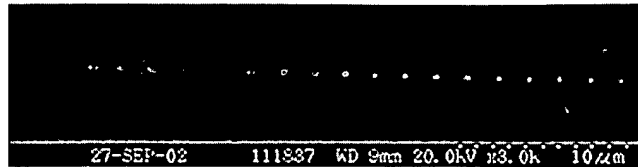


FIGURE 3 A row of holes produced by scanning the laser focus across an inclined Corning 0211 cover glass. The 527-nm laser was focused through a 1.3 NA objective, and the inclination of the cover glass creates a 10-nm displacement of the focus relative to the surface between adjacent holes, as the laser focus progressively sinks into the surface from the left. The maximum width of the holes (~ 200 nm) is approximately the same as the z axis displacement between the first and last holes

(Fig. 4a). This suggests that the laser focus was somewhat below the surface; as the energy approaches threshold, the diameter of the region of ablation becomes small enough that the holes no longer penetrate the surface, and only the larger surrounding features are visible. When experiments were performed using an air objective with a longer depth of focus (NA = 0.65), the threshold is revealed to be the same for the holes and the surrounding features (Fig. 4b).

The reproducibility in terms of the identical size of the features combined with nanometer-size scales indicates that the initial charge carriers that seed avalanche ionization must be created in a very reproducible manner. Such carriers have been theorized to be either pre-existing [12], arising from MPI [1, 7, 12, 15, 16, 19], or from tunneling of electrons through the atomic field potential barrier which is suppressed by the strong electric field of the intense light [12, 15, 16, 19]. Pre-existing carriers cannot explain our results, since the production of holes of such small scale (< 20 nm) and sharp edges (below the resolution of the SEM, i.e. < 4 nm) with regularity and precision would require initial free-electron densities far higher than present in large-band-gap materials – an electron density in excess of 10^{18} e/cm³ is necessary to ensure at least one seed electron in the volume of a hole.

To examine the contribution of MPI to the optical breakdown process, we compared optical breakdown thresholds for linearly polarized (LP) and circularly polarized (CP) pulses. When using tightly focusing high-NA objectives, these comparisons are tricky because it is difficult to ensure that the z axis position of the laser focus is positioned precisely at the sample surface, as is evident from Fig. 4a. Therefore, using the low-NA objective, reproducible features were created using CP and LP pulses of 1053- and 527-nm light.

Material	Wavelength (nm)	LP (nJ)	CP (nJ)	Band gap (eV)
Corning 0211	527	59 ± 3	62 ± 3	Unknown
	1053	1271 ± 75	1305 ± 84	
Silicon	527	5.8 ± 1.1	6.1 ± 1.1	1.1
	1053	172 ± 24	194 ± 20	
Fused silica	527	49 ± 2	57 ± 4	7.1
	1053	907 ± 189	1063 ± 29	
Quartz	527	62 ± 2	56 ± 4	8.4
	1053	950 ± 57	933 ± 88	

TABLE 1 Optical breakdown thresholds for different materials, with LP and CP light at two wavelengths, obtained with 0.65 NA objective

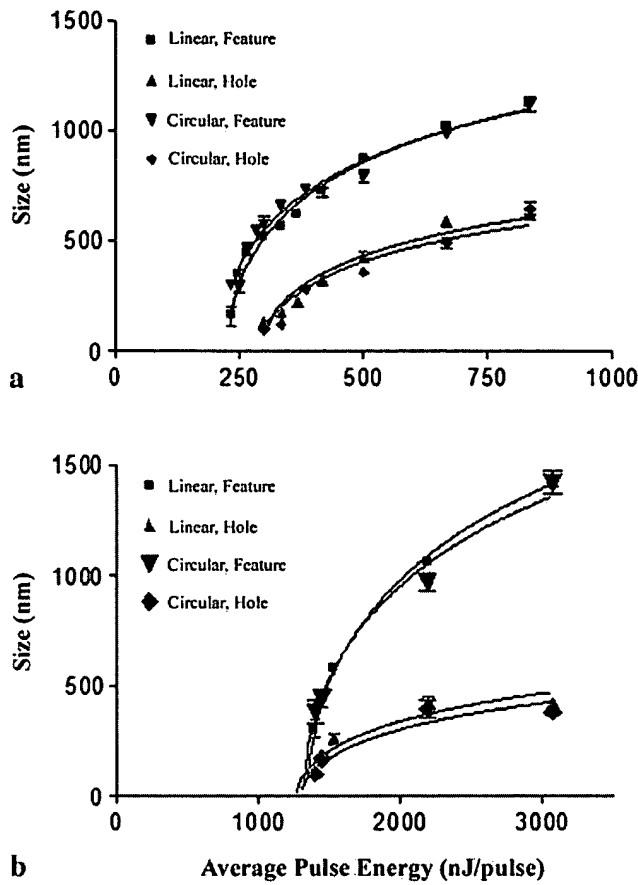


FIGURE 4 Ablation-zone size versus pulse energy. The diameters of both holes and the surrounding features decrease with pulse energy to a sharply delineated threshold below which no damage is observed. Results for linearly and circularly polarized light are shown. Data is fitted with diameter $D = \sigma \sqrt{8 \ln(E/\gamma)}$, where E is pulse energy and γ and σ are fitting parameters. a 1053-nm pulses focused on glass by a 1.3 NA objective. The pulse energy arriving at the sample is substantially less, since the objective is not optimized for near-infrared wavelengths. b 1053-nm pulses focused on glass by a 0.65 NA objective. From the curve fits the values of σ are: linear, hole = 177 ± 20 nm; circular, hole = 163 ± 22 nm; linear, surrounding feature = 552 ± 25 nm; circular, surrounding feature = 523 ± 27 nm

Since it was not difficult to place the focus at the surface of the samples with this long depth of focus lens, the samples were not inclined in these experiments. For either the 1053-nm or 527-nm wavelengths, the threshold energies are independent of the polarization regardless of the material (Table 1). Since CP light is extremely inefficient for producing high-order multiphoton processes, these results largely exclude MPI as a source of initial charge carriers.

Measured by an atomic force microscope (AFM), the depth of holes in glass produced by 1300-nJ pulses of 1053-nm light focused through the 0.65 NA objective was ~ 50 nm, which is in agreement with published observations [2, 3, 15, 19]. This depth represents the extent the region of optical breakdown penetrates the material plus any damage spread due to thermal diffusion. Thus it represents the upper bound of light penetration: the plasma skin depth. This is on the order of the predicted ~ 30 -nm skin depth if all 10^{23} cm^{-3} valence electrons are ionized, indicating complete ionization in the region of the holes.

4 Discussion

We present ultra-high-precision laser machining, a remarkable demonstration of the precision of femtosecond optical breakdown, which reveals a simple approach for manufacturing nanotechnology that can be applied to diverse materials. Even the smallest features are reproducible, and exhibit sharply delineated edges, suggesting that features even more minute might be attained by decreasing the pulse duration or the wavelength. This is made possible by the extremely deterministic character of optical breakdown, which we find is not adequately predicted by existing theory.

Although high-precision applications rely on the deterministic character of femtosecond ablation, this effect has not been extensively studied. It has been modeled in terms of multiphoton-seeded avalanche, yet doubts [20] have been expressed regarding the true importance or necessity of multiphoton effects (championed in [7]). Theories including or describing a significant role for MPI (e.g. [21, 22]) assume a collisionless mechanism where excited electrons do not interact with electrons in neighboring atoms. This is well applied to isolated molecules such as those in gases, but makes less sense in solids. In solids the electron excursions become bigger than the atomic distance and frequent collisions cause dephasing between the electrons and the driving field [4, 20]. This dephasing causes the direction of electron oscillations induced by subsequently absorbed photons to differ, thus diminishing the addition of energy along a given vector that is required for MPI. Likewise, CP light is also expected to be inefficient for inducing MPI because of dephasing caused by rotation of the driving field. Indeed this is observed in gases, in which ionization is much more efficiently produced by LP light, as expected from the conservation of angular momentum of electrons in a non-rotating versus rotating electric field, especially for fourth- or higher-order photon absorption [18]. In this study we examine the mechanism of femtosecond laser-induced optical breakdown near threshold in several different materials using both LP and CP light at 1053-nm and 527-nm wavelengths. Our results show that optical breakdown in solids is independent of the laser polarization, rejecting earlier theories for the deterministic character based on MPI.

The lack of a significant role for MPI suggests that the dominant mechanism for seeding is Zener tunneling of electrons through the atomic field potential barrier, which is suppressed by the strong electric field of the intense light [12, 15, 16, 19]. For avalanche to ensue, the quiver energy of the free electrons must equal or exceed the band gap of the material so that bonds can be broken. The electron quiver energy is given by:

$$E_Q = \left\langle \frac{e^2 E^2}{4m\omega^2} \right\rangle \quad \text{or,} \quad E_Q = 9.3 \times 10^{-14} I \lambda^2, \quad (1)$$

where E_Q is in eV, the intensity I in W/cm^2 , λ in μm , E the laser electric field in V/cm , ω is the angular frequency of the laser, and m is the rest mass of an electron. The importance of E_Q exceeding the band gap is verified by our observation that the threshold scales with the band gap (Table 1). We therefore normalize the electron quiver energy to the band gap through

the coefficient a_0^2 . In this model, a_0^2 marks the transition between pure Zener tunneling to Zener tunneling and avalanche:

$$E_Q = a_0^2 E_g, \quad (2)$$

$$I_g \approx \frac{E_g}{\lambda^2} \approx 10^{13} \text{ W/cm}^2. \quad (3)$$

For $E_Q < E_g$, that is for $I < I_g$, the quiver energy of the electron is insufficient to break bonds, and free electrons are produced by Zener tunneling. Single-photon absorption may also contribute near the surface due to the large number of localized electron states. Similarly, single-photon ionization may also occur at low levels throughout the bulk of an amorphous material such as fused silica or Corning 0211 glass used in this work. From the initial number of valence electrons $N_v = 10^{23} / \text{cm}^3$, the number of electrons n that will tunnel during the laser pulse will be of the order of:

$$n = N_v P \frac{\tau}{\tau_{tu}} N_L, \quad (4)$$

where

$$P = \exp \left(\frac{-4}{3\epsilon h} \sqrt{\frac{2m E_g^3}{E^2}} \right), \quad (5)$$

and

$$\tau_{tu} = \frac{\sqrt{2m E_g}}{eE} = \frac{\tau}{a_0 \sqrt{2}}, \quad (6)$$

with τ_{tu} being the tunneling time, τ the laser period, P the tunneling probability, N_L is the number of laser periods, and h is the Planck constant. P can be expressed in terms of the normalization parameter a_0 and ν the laser frequency:

$$P = \exp \left(\frac{-4}{3\sqrt{2a_0}} \frac{E_g}{h\nu} \right). \quad (7)$$

Therefore, the number of free electrons in the conduction band is given by:

$$n = a_0 N_L N_v \exp \left(\frac{-4}{3\sqrt{2a_0}} \frac{E_g}{h\nu} \right). \quad (8)$$

For $a_0 < 1$, that is, below threshold for avalanche, this probability is small but the valence-electron density is large, $10^{23} / \text{cm}^3$, which can lead to a significant number of free electrons tunneling to the conduction band. For $a_0 \geq 1$, the tunneling time is of the order of or greater than the laser period. The electrons are energetic enough to break bonds, and avalanche ionization ensues. For a 10-eV gap and a 1-eV photon, about one thousandth of the valence electrons will tunnel each period. Thus, even for a large band gap and a low photon energy, after 10 to 100 periods a significant fraction of the electrons will have tunneled through the gap. The electron energy is such that collisions are frequent, and tunneling is quickly followed by avalanche ionization that exhausts all available valence electrons, as indicated by the $\sim 50\text{-nm}$

ablation depth. Note that electrons are produced by Zener tunneling and avalanche in a manner very similar to device electronics such as Zener diodes, where they proceed simultaneously, and are impossible to differentiate.

Though this picture suggests that the relation between threshold and band gap is explained by the required energy to induce avalanche (i.e. $a_0 \geq 1$), the origin of the extremely deterministic behavior is still unclear. If optical breakdown coincided purely with the onset of avalanche, variability in the band-gap structure should be apparent as variability in the observed damage. But no such variability is observed; even in materials with substantially variable band structure such as Corning 0211 or fused silica [23], reproducible features are produced at small scales with sharp edges. We propose that avalanche ionization is a necessary prerequisite for optical breakdown, but in of itself is not sufficient. Breakdown occurs some time after the onset of avalanche, when the electron density rises precipitously as the plasma frequency approaches the laser frequency and the absorption of laser energy is strongly enhanced. The following picture emerges. The seed charge carriers (free electrons) are first created in a confocal volume at or near the substrate surface by single-photon absorption or tunneling. In practice tunneling will be enhanced by the variability of the surface states (i.e. band bending). When the carrier energy becomes greater than the band gap, the carriers are further multiplied by impact ionization. The time between collisions τ decreases as the electron energy increases to become of the order of a fraction of a femtosecond for energies of the order of 1 eV. The increase in free-electron density sharply augments the plasma frequency ω_p , and decreases the dielectric constant ϵ to near zero when the plasma frequency reaches the laser frequency:

$$\epsilon = \epsilon_{\text{bound}} \left[1 - \left(\frac{\omega}{\omega_p} \right)^2 \right] \quad \text{with} \quad \omega_p^2 = \frac{4\pi n e^2}{m}. \quad (9)$$

Here ϵ_{bound} is the contribution of the bound electrons. For $a_0 < 1$, ϵ_{bound} will be assumed constant, as the number of free electrons represents a very small fraction of the total (bound + free). The electric field in the plasma is equal to E/ϵ . When the plasma frequency approaches the laser frequency ω , the electric field experiences a strong enhancement, further increasing impact ionization. This produces a runaway process that terminates when all the valence electrons are ionized. Since n depends on the total electron density, which is uniform and independent of the gap throughout the material, even at the nanometer scale the susceptibility to this process is invariant across the material, even if the band structure is not, as is the case for Corning 0211 or fused silica [23]. When the plasma frequency becomes greater than the laser frequency, the plasma screens the electric field and becomes strongly absorbing. The laser light is absorbed over a plasma skin depth δ given by:

$$\frac{c}{\omega_p} > \delta > \frac{c}{\omega_p \left(\frac{1}{2} \omega \tau \right)^{\frac{1}{2}}}. \quad (10)$$

For 10^{23} e/cm^3 this skin depth is of the order of 30 nm.

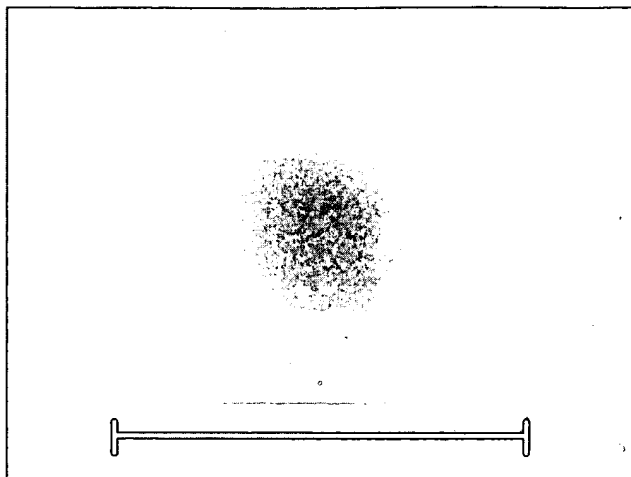


FIGURE 5 SEM of a hole in a cell membrane. Chinese Hamster ovary cells were cultured on cover slips and fixed with gluteraldehyde before laser ablation by 1053-nm pulses focused through a 1.3 NA objective (scale bar = 500 nm)

The material exhibits metallic character in the absorbing volume, and the interaction is over-critical with a low plasma temperature of several eV set by the bond-breaking energy. The over-critical spot area being completely metallic, the situation becomes analogous to the interaction with metals where sub-wavelength damage has been demonstrated [9]. After a few picoseconds, the electrons transfer their kinetic energy to the ions. Once the kinetic energy of the ions is sufficient to move them by a fraction of the lattice constant, the material undergoes a phase transition and melts. Note that in the case of short pulses, absorption occurs within the material as opposed to a long pulse where the absorption also occurs at a distance from the surface due to plasma expansion.

Thus, optical breakdown by ultra-fast lasers depends on a process that begins with Zener, continues with combined Zener and impact ionization, but culminates through absorption of laser energy in a sharply delineated volume of completely ionized material. The deterministic character of the optical breakdown is dictated by the material valence-electron spatial uniformity. It is neither determined by the initial electron band-gap distribution, nor the initial free-electron distribution, both of which are not sufficiently uniform over observed 20-nm features to explain the observed reproducibility. Note that in good-quality optical material the energy gap may vary substantially over small scales but the valence-electron density, which is proportional to the atomic density, is extremely uniform.

The highly reproducible nature of this mechanism allows for ultra-high-precision laser machining that is simple, robust, and can create features ranging from microns to the low end of the nanometer scale. These aspects make it a simple matter to form more complicated structures by repeatedly machining holes at different locations. As an example of this production process, we have machined pipes of nanoscale diameters that are many microns long by repeatedly firing pulses at a glass target while displacing its z axis position. For more rapid pro-

cessing, a system for scanning the focus of multiple beams in three dimensions could be applied (e.g. [24]). The technique is versatile; it does not require specific materials, and for many applications it is simpler and more reliable compared with other methods capable of producing features on this size scale (e.g. electron-beam lithography and nanoimprinting). This enabling technology has potentially broad applications for MEMS construction and design, ultra-high-density microelectronics, nanofluidics, materials science, optical memory, and the creation of structures to interface with cells and biological molecules. It can also extend the utility of ultra-fast lasers in biology [11]. We have applied ultra-high-precision laser machining to produce well-defined ablations in cells (Fig. 5), and anticipate that it will have great impact in the biological sciences, including research in cell motility, development, growth-cone and neurite extension, and targeted disruption of genetic material.

ACKNOWLEDGEMENTS We would like to acknowledge and thank Dr. T. Juhasz and IntraLase, Corp., for making available the femtosecond laser source used in this work. We thank A. Mecke for the AFM analysis and Dr. J. Singh for discussions regarding avalanche ionization and its importance to Zener diodes. This work was supported by grants to AJH from the National Science Foundation and the Burroughs Wellcome Fund. GAM is supported by NSF and Michigan Economic Development Corporation.

REFERENCES

- 1 D. Du, X. Liu, G. Korn, J. Squier, G. Mourou: *Appl. Phys. Lett.* **64**, 3071 (1994)
- 2 E.N. Glezer, M. Milosavljevic, L. Huang, R.L. Finlay, H.H. Her, J.P. Callan, E. Mazur: ed. by P.F. Barbara (Springer, New York 1996) p. 157
- 3 W. Kautek, J. Krueger: *Mater. Sci. Forum* **173–174**, 17 (1995)
- 4 X. Liu, D. Du, G. Mourou: *IEEE J. Quantum Electron.* **QE-33**, 1706 (1997)
- 5 C. Momma, B.N. Chichkov, S. Nolte, F. Alvensleben, A. Tunnermann, H. Welling, B. Wellinghausen: *Opt. Commun.* **129**, 134 (1996)
- 6 S. Nakamura, T. Okamoto, H. Kumagai, K. Midorikawa, M. Obara, K. Toyoda: *Appl. Phys. Lett.* **65**, 1850 (1994)
- 7 B. Stuart, M. Feit, A. Rubenchik, B. Shore, M. Perry: *Phys. Rev. Lett.* **74**, 2248 (1995)
- 8 D. Du, J. Squier, R. Kurtz, V. Elner, X. Liu, G. Gutmann, G. Mourou: ed. by P.F. Barbara (Springer, New York 1995) p. 254
- 9 P. Pronko, S. Dutta, J. Squier, J. Rudd, D. Du, G. Mourou: *Opt. Commun.* **114**, 106 (1995)
- 10 K. Venkatakrishnan, B. Tran, P. Stanley, N. Sivakumar: *J. Appl. Phys.* **92**, 1604 (2002)
- 11 K. Konig, I. Riemann, W. Fritzsche: *Opt. Lett.* **26**, 819 (2001)
- 12 N. Bloembergen: *IEEE J. Quantum Electron.* **QE-10**, 375 (1974)
- 13 J. Squier, F. Salin, G. Mourou, H.H. Her: *Opt. Lett.* **16**, 324 (1991)
- 14 K.K. Thornber: *J. Appl. Phys.* **52**, 279 (1981)
- 15 M. Lenzner, S. Kruger, S. Sartania, Z. Cheng, C. Spielmann, G. Mourou, W. Kautek, F. Krausz: *Phys. Rev. Lett.* **80**, 4076 (1998)
- 16 A. Tien, S. Backus, H. Kapteyn, M. Murnane, G. Mourou: *Phys. Rev. Lett.* **82**, 3883 (1999)
- 17 D. Du: Doctoral Thesis, Physics, University of Michigan (1996)
- 18 L. Lompré, G. Mainfray, C. Manus, J. Thebault: *Phys. Rev. A* **15**, 1604 (1977)
- 19 C. Schaffer, A. Brodeur, J. Garcia, E. Mazur: *Opt. Lett.* **26**, 93 (2001)
- 20 D. Du, X. Liu, G. Mourou: *Appl. Phys. B* **63**, 617 (1996)
- 21 A. Kaiser, B. Rethfeld, M. Vicanek, G. Simon: *Phys. Rev. B* **61**, 437 (2000)
- 22 L. Keldysh: *Sov. Phys. JETP* **20**, 1307 (1965)
- 23 J. Fritzsche: *J. Non-Cryst. Solids* **6**, 49 (1971)
- 24 G.J. Brouhard, H.T. Schek, A.J. Hunt: *IEEE Trans. Biomed. Eng.* **50**, 121 (2003)

First Clinical Results With the Femtosecond Neodymium-glass Laser in Refractive Surgery

Imola Ratkay-Traub, MD, PhD; Istvan E. Ferincz, MSc; Tibor Juhasz, PhD; Ron M. Kurtz, MD; Ronald R. Krueger, MD, MSE

ABSTRACT

PURPOSE: We evaluated four femtosecond laser intrastromal cutting procedures: creation of a corneal flap for laser *in situ* keratomileusis (LASIK), tunnel and entry cut for intracorneal ring, corneal flap and removable lens for keratomileusis, and intrastromal ablation for myopia and hyperopia.

METHODS: A clinical trial using a femtosecond surgical laser (IntraLase Corporation) was performed in partially sighted eyes. Femto-LASIK treatment was performed on 46 eyes up to -14.00 D; 16 patients received intracorneal ring segments (Femto-ICRS); 5 patients each with one highly myopic eye had femtosecond laser keratomileusis (FLK), and 13 patients each with one myopic or hyperopic eye had intrastromal ablation (ISPRK). In Femto-LASIK, excimer laser ablation was done under the flap. In Femto-ICRS, ring segments were introduced into the laser-created channels. In femtosecond laser keratomileusis, a lens-shaped block of stroma was removed manually from under the flap.

RESULTS: No difference was found between the results obtained with Femto-LASIK and a standard microkeratome. No refractive effects occurred when the created flap was not elevated. In cases of Femto-ICRS and conventional ICRS produced the same refractive results. With Femto-ICRS, no intraoperative complications occurred and visual acuity improved immediately after surgery. In femtosecond laser keratomileusis, high myopia was corrected without using excimer laser ablation; centralization of the treatment area was excellent. In intrastromal ablation, 1 to 2 hours after surgery the corneas were highly transparent; refractive results were stable.

CONCLUSIONS: Femtosecond lasers can produce precise intrastromal cutting, offering significant safety and other advantages (no razor blades, corneal trauma, partial resections, or sterilization issues) over current techniques. [J Refract Surg 2003;19:94-103]

From the Focus Medical Eye Micro-surgery and Laser Center, Budapest, Hungary (Ratkay-Traub); the Department of Optics and Quantum Electronics, University of Szeged, Szeged, Hungary (Ferincz); the Department of Biomedical Engineering, University of Michigan, Ann Arbor, MI (Juhasz); IntraLase Corporation, Irvine, CA (Juhasz, Kurtz); the Department of Ophthalmology, University of California, Irvine, CA (Kurtz); and the Cole Eye Institute, Cleveland Clinic Foundation, Cleveland, OH (Krueger).

This research received grant support from the National Science Foundation (STC/PHY 8920108) National Institute of Health (N.E.I. Core Grant EY-00703, IR43EY12340-01), U.S. Air Force (F29601-98-C-0146), a grant in Hungary from ETT 182/97, the University of Michigan Kellogg Eye Center (Ann Arbor, MI), and IntraLase Corporation (Irvine, CA).

Tibor Juhasz and Ron Kurtz are employees of IntraLase Corporation, a company commercializing devices and procedures discussed in this article.

We gratefully acknowledge our technical staff and coworkers, including Drs Krisztina Kiss, Christopher Horvath, Carlos Suarez, and also Professor David Schanzlin, for his participation and helpful discussions.

Correspondence: Imola Ratkay-Traub, MD, PhD, Focus Medical Eye Micro-surgery and Laser Center, H-1138 Budapest, XIII, Danubius Thermal Hotel Margitsziget, Hungary. Tel: 36.1.450 3333; Fax: 36.1.450 3331; E-mail: traubfri@axelero.hu

Received: January 30, 2002

Accepted: September 18, 2002

Neither visible or near infrared laser light are absorbed by the refractive structures of the eye at low power densities, allowing the light to freely pass into the eye without any surgical cut or effect. At high power densities, the non-linear optical properties of these structures lead to absorption, generating plasma.^{1,2} The infrared Neodymium-glass femtosecond laser emits a wavelength similar to the Neodymium-YAG laser, which is used widely in ophthalmic laser surgery.³ Each femtosecond laser pulse is approximately ten thousand times shorter in duration, compared to a Q-switched Nd:YAG laser, and lasts only about 10 to 13 seconds.^{1,4,5}

Unlike photothermal lasers, the high peak intensities of the femtosecond laser allows it to create a plasma inside transparent tissues—such as the cornea—without interfering with surface cell layers (Fig 1). Femtosecond laser pulses require significantly less energy to produce photodisruption compared to longer pulsed lasers, such as the picosecond and nanosecond laser.⁶⁻⁸ This lower energy threshold translates into smaller cavitation

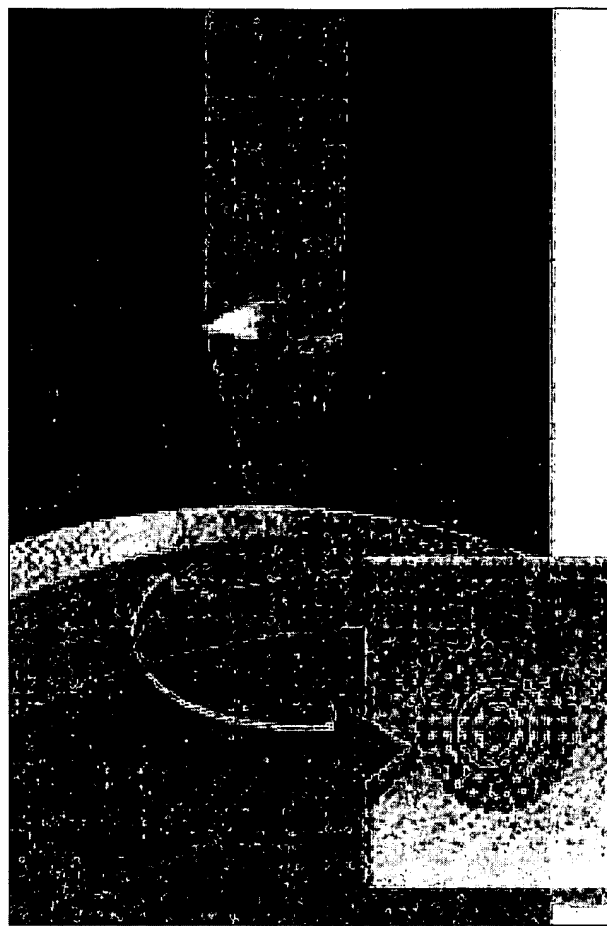


Figure 1. Intrastromal surgery with a scanning femtosecond laser places pulses inside the cornea without interfering with the surface layers (courtesy IntraLase Corporation, Irvine, CA).

bubble size (microcavitation) (Table 1), allowing nearly contiguous placement of laser pulses. Computer-controlled, high-precision delivery system optics, capable of scanning the focused beam over a 10-mm working diameter with micron-range accuracy have been developed, making these ultrafast lasers ready for biological and medical applications. In cooperation with the University of Michigan at Ann Arbor, MI and the IntraLase Corporation (Irvine, CA), we performed the first clinical studies with the α -prototype of the Pulsion FS equipment to demonstrate the efficacy of this laser in ophthalmic surgery.

We also performed *ex vivo* and *in vivo* animal studies for potential corneal applications, which led to human clinical trials (Fig 2).^{8,9} In this report, we summarize our long-term follow-up experience with this Pulsion FS laser prototype in making flaps

Table 1
Fluence Threshold, Shockwave Range, and
Cavitation Bubble Diameter in the Cornea
as a Function of Laser Pulse Duration

Pulse Duration	150 fs	500 fs	60 ps	10 ns
Threshold fluence (J/cm ²)	~1.5	~1.6	14	~185
Shock wave range (μm)	~20	20	~200	~700
Cavitation bubble diameter (μm)	3 to 15	3 to 15	30 to 120	300 to 1200

(Femto-LASIK), creating intrastromal tunnels for intrastromal corneal ring segments (Femto-ICRS), femtosecond laser keratomileusis with lenticule removal (FLK), and intrastromal photorefractive keratectomy (ISPRK) in which corneal tissue is removed without disturbing the epithelium.

PATIENTS AND METHODS

Laser Procedure

The femtosecond laser is an Nd:glass laser that operates at 1.05 μm wavelength, and emits 500 fs pulses at a 3 to 5 kHz repetition rate. The typical pulse energy is between 4 and 6 mJ. Alignment of the system is first verified on a test surface. After placement of topical anesthetic and antibiotic drops, a lid speculum is inserted to achieve sufficient exposure. A suction ring is then applied to the limbus, and a contact lens assembly is used to appenate the cornea. During appenation, the intraocular pressure is elevated to approximately 35 mmHg. The laser pulses are delivered according to pre-programmed patterns for creation of a flap, lenticule, channel, or for volumetric reduction during intrastromal photorefractive keratectomy.

Studies in Pig Eyes: Accuracy and Reproducibility of Femtosecond Laser Resections

Flap creation was tested in fresh porcine eyes for accuracy and reproducibility of resections. Although the system can deliver a wide range of resection parameters, initially flaps of 8.5 mm, 9.0 mm, and 9.5 mm were evaluated at a single depth of 160 μm. A series of resections at varying depths were also evaluated at a single diameter. A digital micrometer (Starrett, model 788, Athol, MA) was used to measure flap thickness with the flap held between two glass slide covers. Bed diameter was measured as the largest distance passing through the corneal center. As seen in Table 2, flap thickness and

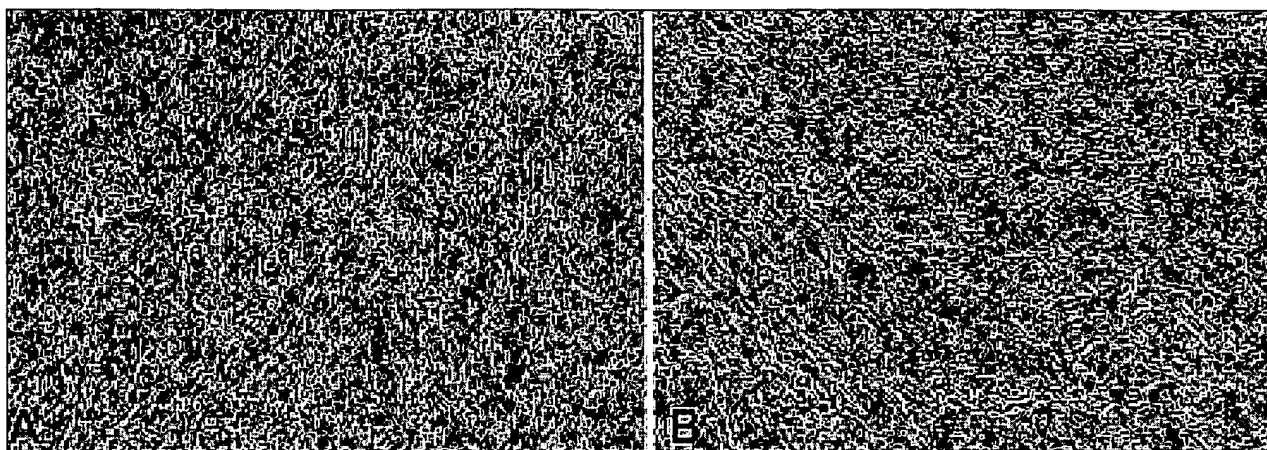


Figure 2. Scanning electron micrographs of the corneal flap interface created with A) mechanical keratome (Chiron Hansatome), and B) femtosecond laser keratome in ex vivo porcine corneas. The surface quality of the corneal bed produced by the laser is at least equivalent or slightly smoother than that of the mechanical keratome. Magnification $\times 200$.

Table 2
Flap Thickness and Diameter Reproducibility at 160- μ m Setting
With the Femtosecond Laser

Intended Flap Diameter (25 eyes per group)	9.5-mm Resection	9.0-mm Resection	8.5-mm Resection
Achieved flap diameter (mm) (mean \pm SD)	9.4 \pm 0.1	9.0 \pm 0.1	8.6 \pm 0.1
Percentage of variance (%)	1.1	1.1	1.2
Percentage of variation from intended (%)	1.1	0	1.2
Intended flap thickness (μ m)	160	160	160
Achieved flap thickness (μ m) (mean \pm SD)	162 \pm 13	165 \pm 11	156 \pm 10
Percentage of variance (%)	8.0	6.7	6.4
Percentage of difference from intended (%)	1.3	3.1	2.5

diameter were highly reproducible and accurate. Flap thickness varied from 6% to 8%, or approximately 12 μ m at the intended 160- μ m resection thickness. Flap diameter was also reproducible, achieving values in the 1% to 3% range, which means approximately 0.1 to 0.3 mm deviation from the intended diameter.

Femto-LASIK

For corneal flaps, an outwardly expanding spiral pattern consisting of approximately 500,000 to 800,000 pulses was scanned at 160, 180, or 200 μ m depth for a total diameter of 8 to 10 mm. This was followed by a side cut to the surface, with creation of a hinge by partially blocking the beam. After completion of the laser procedure, suction was released and the contact lens delivery system was elevated, allowing access to the resected corneal flap. Excimer laser photoablation (VISX 20/20B, Santa Clara, CA) was then performed under the elevated flap. The flap was then repositioned, as with conventional LASIK, and the edges were aligned easily due to the

cone-shaped edge cut made at 45° relative to the surface.

Femto-ICRS

For a channel, a spiral was used to create an expanding annular pattern using approximately 200,000 pulses at a depth of 400 μ m (approximately two-thirds corneal depth) with an inner ring diameter of 6.6 mm and an outer diameter of 8.2 mm. Intrastral corneal ring segments (ICRS, KeraVision, Fremont, CA) were then introduced into the laser-created channels, after dissection of the interface with a blunt instrument.

Femtosecond Laser Keratomileusis

For a lenticule, a plano-convex lens-shaped volume of corneal stroma was laser resected by first introducing an expanding spiral in a concave pattern, relative to the corneal surface, to a diameter of 4.5 mm. A central depth of 60 μ m more than the intended flap thickness and a peripheral depth at the level of the flap thickness allowed for an

-8.50-diopter (D) myopic refractive correction. A corneal flap was then created, as with Femto-LASIK, after which the lenticule was identified and removed manually from below the flap. Finally, the flap was repositioned easily, as with Femto-LASIK.

Intrastromal Photorefractive Keratectomy

For intrastromal volume reduction, leaving the epithelium intact, the suction ring and contact lens delivery system were once again applied. In these early experiments, we used a truncated cone-shaped pattern for myopia and a ring-shaped pattern for hyperopia treatment, in order to examine refraction changes without disturbing the central part of the cornea. For correction of myopia, a total of 7 to 10 lamellar layers of laser pulses were focused starting at a corneal depth of 170 to 200 μm and ending 100 μm from the surface. The most posterior layer of pulses was applied to a diameter of 3.5 mm. With each successive layer placed 10 μm more anterior to the next, the diameter was enlarged an additional 0.3 to 0.42 mm, so that the final most anterior layer had a diameter of 6.5 mm. For correction of hyperopia, 7 to 10 ring layers were applied with an inner diameter of 6.0 mm and an outer diameter of 8.0 mm. Since an individual femtosecond laser pulse is estimated to remove a volume of 27 to 125 μm^3 by converting collagen to a gas through plasma mediated ablation, the total depth of tissue removed should correspond to the pulse volume times the number of layers and take on a profile dependent on the diameter of each layer.

After the procedures, eyes received a combined topical antibiotic/anti-inflammatory agent (Tobra-Dex, Alcon, Ft Worth, TX) and a holed patch for 1 day. Postoperatively, these drops were used five times per day for 1 week, and then three times per day for 1 month. Topical artificial tears were also used five times per day for 1 to 3 months. Follow-up examinations were performed 1 day, 1 week, and 1, 3, 6, 12, and 18 months after femtosecond laser refractive surgery.

Patient Enrollment

Both fully sighted and partially sighted eyes were enrolled for this initial clinical evaluation of femtosecond laser refractive surgery. The procedures were performed in only one eye of each patient, except in the Femto-LASIK and Femto-ICRS groups, where several patients had both eyes (sighted) done 1 to 3 months apart.

For Femto-LASIK, surgery was performed on 46 eyes (24 OD, 22 OS) for myopia up to -14.00 D.

Patient age range was 23 to 55 years (mean 36.93 \pm 10.3 yr); there were 30 females and 16 males.

For Femto-ICRS, 16 eyes (7 OD, 9 OS; 8 male, 8 female) received the channel-forming treatment with implantation of intrastromal corneal ring segments. Patient age range was 31 to 50 years (mean 39.8 \pm 6.5 yr).

For femtosecond laser keratomileusis, five eyes of five patients, each with one highly myopic, anisotropic and amblyopic eye, were sculpted by the femtosecond laser to create and remove a corneal lenticule from the amblyopic eye. Patient age range was 20 to 43 years (mean 29 \pm 11.1 yr).

For intrastromal photorefractive keratectomy, the procedure was performed in 13 patients, each with an amblyopic eye (4 myopic, 9 hyperopic). Patient age range was 21 to 54 years (mean 35 \pm 11.1 yr).

Four patients in the Femto-LASIK group and one in the Femto-ICRS group were selected as controls, with no secondary refractive procedure (excimer ablation or ring insertion). These were selected in order to evaluate potential refractive effects of the femtosecond laser procedure itself.

Preoperative and postoperative examinations included slit-lamp microscopy, Schirmer strip, tear break-up time, corneal topography, ultrasonic biometry and pachymetry, direct and indirect ophthalmoscopy, uncorrected (UCVA) and best spectacle-corrected Snellen visual acuity (BSCVA) and manifest and cycloplegic refraction; follow-up time was at least 1 year.

RESULTS

Femto-LASIK

In the 43 patients who had flap creation with the femtosecond laser (Fig 3) followed by excimer laser treatment, refractive results achieved were comparable to those of the conventional LASIK procedure, performed by the same surgeon.

Figure 4 shows BSCVA change over 1.5 years of follow-up after the femtosecond-LASIK treatment. We treated amblyopic eyes, so the average BSCVA was just slightly above 20/40. This figure suggests that the wound healing process was slower compared to conventional LASIK, and may be explained by difficulties encountered in flap elevation; in a few eyes separation of the flap from the stromal bed was not optimum. Figure 5 shows change in BSCVA at 6 months compared to before surgery. No patient lost two or more lines of BSCVA and most patients (36 of 43; 83.7%) attained a postoperative

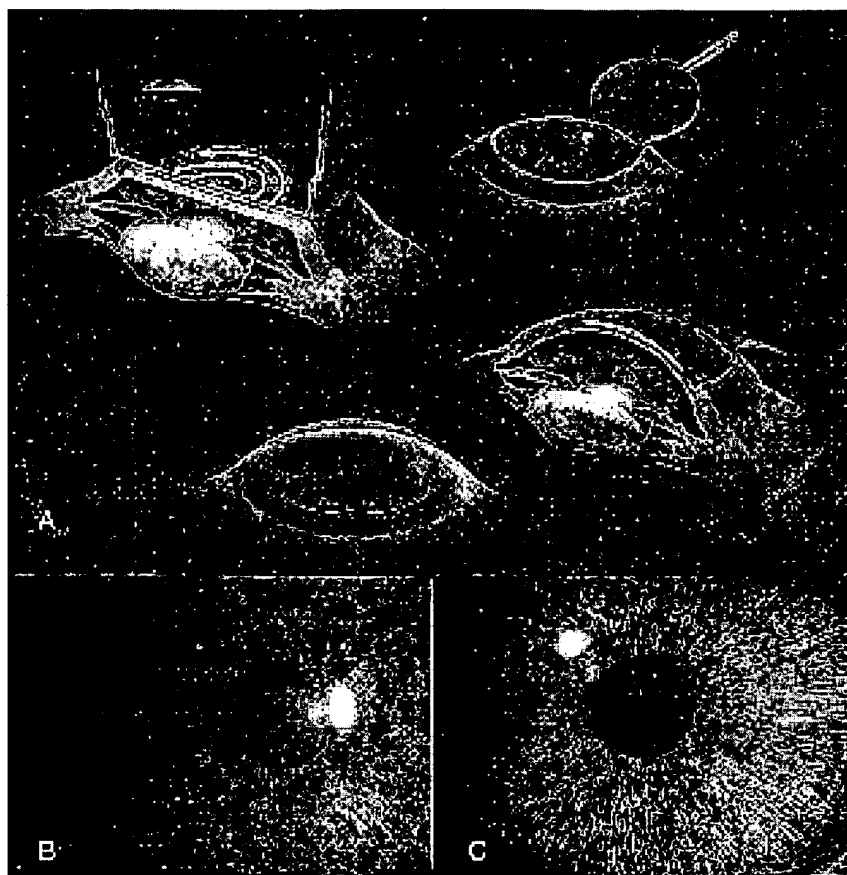


Figure 3. **A)** Steps of corneal flap creation with a femtosecond laser keratome (courtesy IntraLase Corporation, Irvine, CA). **B)** Post-operative slit-lamp photomicrographs at 12 hours after surgery, and **C**) at 1 week after surgery show no loss of corneal clarity and excellent flap stability.

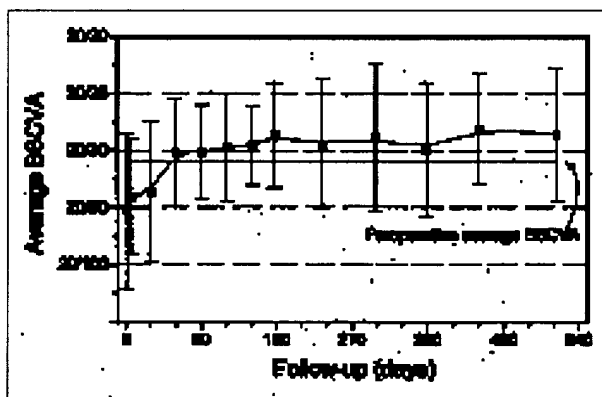


Figure 4. Change in best spectacle-corrected visual acuity (BSCVA) over time after Femto-LASIK in 46 eyes.

uncorrected visual acuity equal to their preoperative BSCVA.

Achieved (6 mo after surgery) versus intended refractive correction is presented in Figure 6. The highly myopic eyes show undercorrection, but none of the eyes were overcorrected by more than 1.00 D. The slope of the fitted line is 0.856 shows good cor-

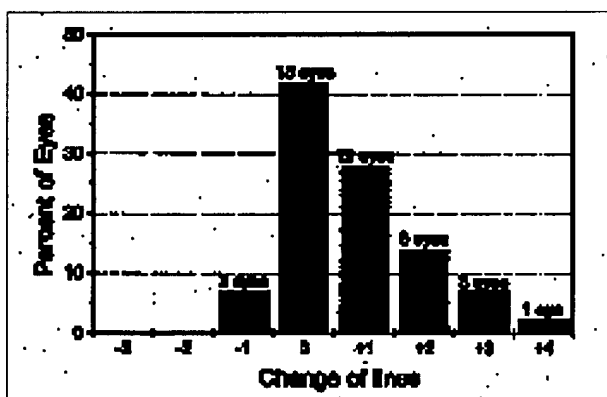


Figure 5. Change in Snellen lines of BSCVA 6 months after Femto-LASIK compared to before treatment in 46 eyes.

relation (correlation coefficient, $R=0.9855$) compared to our conventional LASIK-treated eyes performed with a Hansatome microkeratome (Chiron/Bausch & Lomb, Rochester, NY) and VISX 20/20 B excimer laser. In six eyes with high myopia, the full excimer laser ablation was not performed in order to leave a sufficient residual corneal stromal

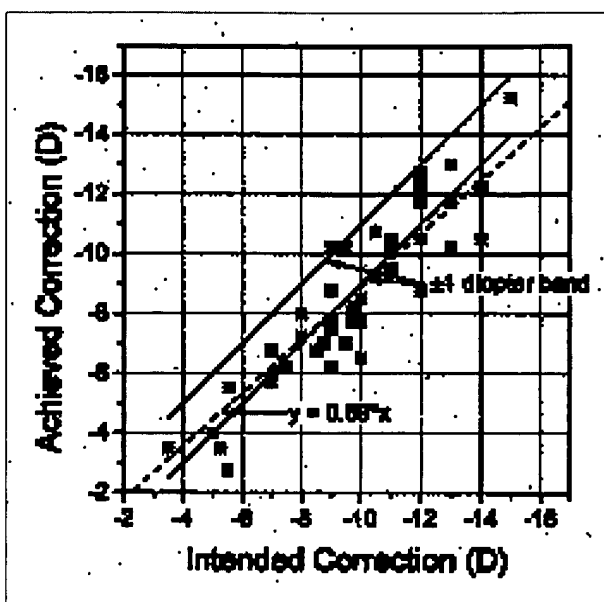


Figure 6. Achieved versus intended correction at 6 months follow-up after Femto-LASIK in 46 eyes.

bed. In three eyes, the flap was cut but not lifted; no change was seen in manifest refraction or corneal topography. Figure 7 shows change in average manifest refraction during the same follow-up period.

Minor complications included decentration of the flap (two eyes) because of imperfections in the applanation device (patient interface). The magnitude of the decentrations was less than 2 mm, thus excimer laser photoablations were performed. In these cases we were not able to maintain the centration of the vacuum ring that holds the patient's eye during treatment. On the basis of these experiences, the patient interface has been improved. Three early patients also developed epithelial inclusion cysts between the flap edge and adjacent stroma, when the edge was perpendicular to the corneal surface. This was due to mild retraction of the edge from the adjacent stroma; this improved after changing the vertical flap edge to an edge with an angle 45° from the surface. Free caps or buttonholed flaps, which are occasionally seen when using a traditional microkeratome, were not observed. There was no epithelial ingrowth in the interface and no further epithelial inclusion cysts after changing the flap edge orientation. The flaps created with the femtosecond laser were more uniform in thickness than traditional flaps. We measured flap thickness in vivo in 15 eyes with the Advent ultrasound pachymeter (Mentor, Norwell, MA). Flap thickness was evaluated by subtracting the thickness of the

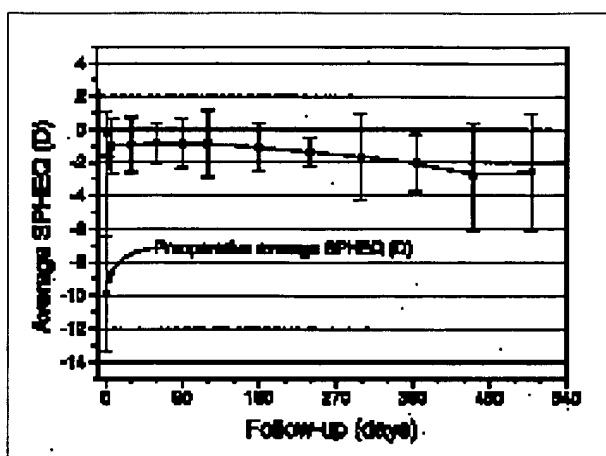


Figure 7. Change in spherical equivalent refraction during follow-up after Femto-LASIK in 46 eyes.

residual stromal bed from preoperative corneal thickness. Mean thickness value was $159 \pm 8.5 \mu\text{m}$; intended value was 160 μm . This result correlates strongly with a more detailed in vitro study (Table 2). The percentage of difference from the average in the in vitro study is 1.9%. The resected flaps showed excellent stability immediately after repositioning (Fig 3), without loss of corneal clarity. As multiple procedures were performed, we were able to optimize dissection and surface quality, side cut, hinge architecture, and centration techniques.

Femto-ICRS

In the 16 patients where intrastromal corneal ring segments were implanted into tunnels made with the femtosecond laser (Fig 8), refractive results were the same as with the standard ICRS procedure. However, unlike conventional ICRS, there were practically no operative complications. We found only minimal deposits in the tunnels in two eyes in the first postoperative month, and these deposits did not get more prominent over the following year. Visual acuity improved immediately after surgery (Fig 8).

Femtosecond Laser Keratomileusis

In five patients (five eyes) who had femtosecond laser keratomileusis, mild corneal edema occurred during the first 2 postoperative days. Centration of the procedures was excellent and the high amount of myopia in these amblyopic eyes was corrected following removal of the lenticule (Fig 9). Corneal transparency was maintained, and refractive stability was good (Fig 9). Uncorrected visual acuity was better than preoperative BSCVA in all patients.

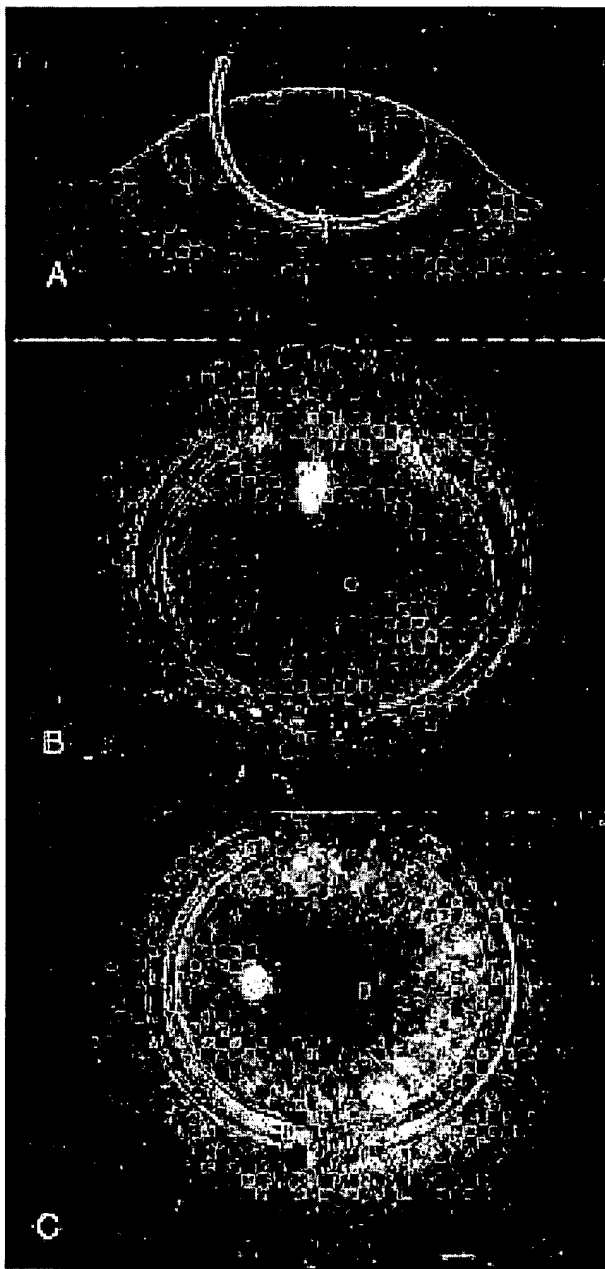


Figure 8. Pre-cut channels and entry cuts made by the femtosecond laser for corneal implants. **A**) Pulses are scanned in a circular pattern below the surface to create the channel, followed by an entry cut for inserting the implants. Slit-lamp photomicrographs (courtesy IntraLase Corporation, Irvine, CA) **B**) immediately after intracorneal ring implantation, and **C**) 1 day postoperatively.

Intrastromal Photorefractive Keratectomy

Intrastromal photorefractive keratectomy of the cornea was performed in five moderately myopic-amblyopic, and eight hyperopic-amblyopic eyes. The bubbles created during surgery in the stroma

disappeared within 1 to 2 hours after surgery (Fig 10), after which the corneas became highly transparent. Figure 11 shows the pattern of pulse placement and topographic change for both myopic and hyperopic eyes. Refractive results for the hyperopic patients were stable by the first month; they achieved a mean correction of +2.00 D postoperatively (Fig 12). Visual acuity (with and without correction) in every eye was better at 1 week after surgery compared to preoperative BSCVA. For the high myopic and amblyopic patients, refractive results improved more slowly; they achieved a stable mean correction of -1.00 D at 3 months, -1.25 D at 6 months, and -2.25 D at 12 months postoperatively (Fig 13). There was no haze detected throughout the 18 months of follow-up; fluoromethalone eye drops were used during the first postoperative month.

DISCUSSION

Laser in situ keratomileusis using a microkeratome to create a corneal flap^{10,11} has been the most commonly performed surgical procedure worldwide for correcting refractive errors.¹²⁻¹⁴ Although LASIK has a high success rate, complications have been reported in approximately 2% to 6% of eyes^{15,16} with visually significant consequences in about 10%. The majority of these are linked to deficiencies in microkeratome performance.

Our initial experience with the femtosecond laser surgical system reveals a number of clinical advantages over traditional techniques. For example, corneal flap creation with a mechanical microkeratome can lead to the unique disadvantage of thin, thick, irregular, button-holed, or partial flaps, as well as metal fragment deposits.^{15,16} The reproducibility and ability to vary laser-created parameters (such as thickness, diameter, hinge location, hinge angle, and side-cut architecture), as well as maintain normal intraocular pressure, can facilitate greater clinical safety and flexibility.^{1,20}

The flaps we created in animal experiments and in the human clinical trials displayed excellent stability immediately after repositioning, without loss of corneal clarity. Pulse spacing and refinement can optimize the dissection, surface quality, side cut and hinge architecture, as well as centration techniques.

We have demonstrated that a femtosecond laser can be used for implanting intrastromal corneal rings with similar results to those of traditional ICRS.¹⁷

In the case of femtosecond laser keratomileusis, the anterior curvature of the cornea flattens due to

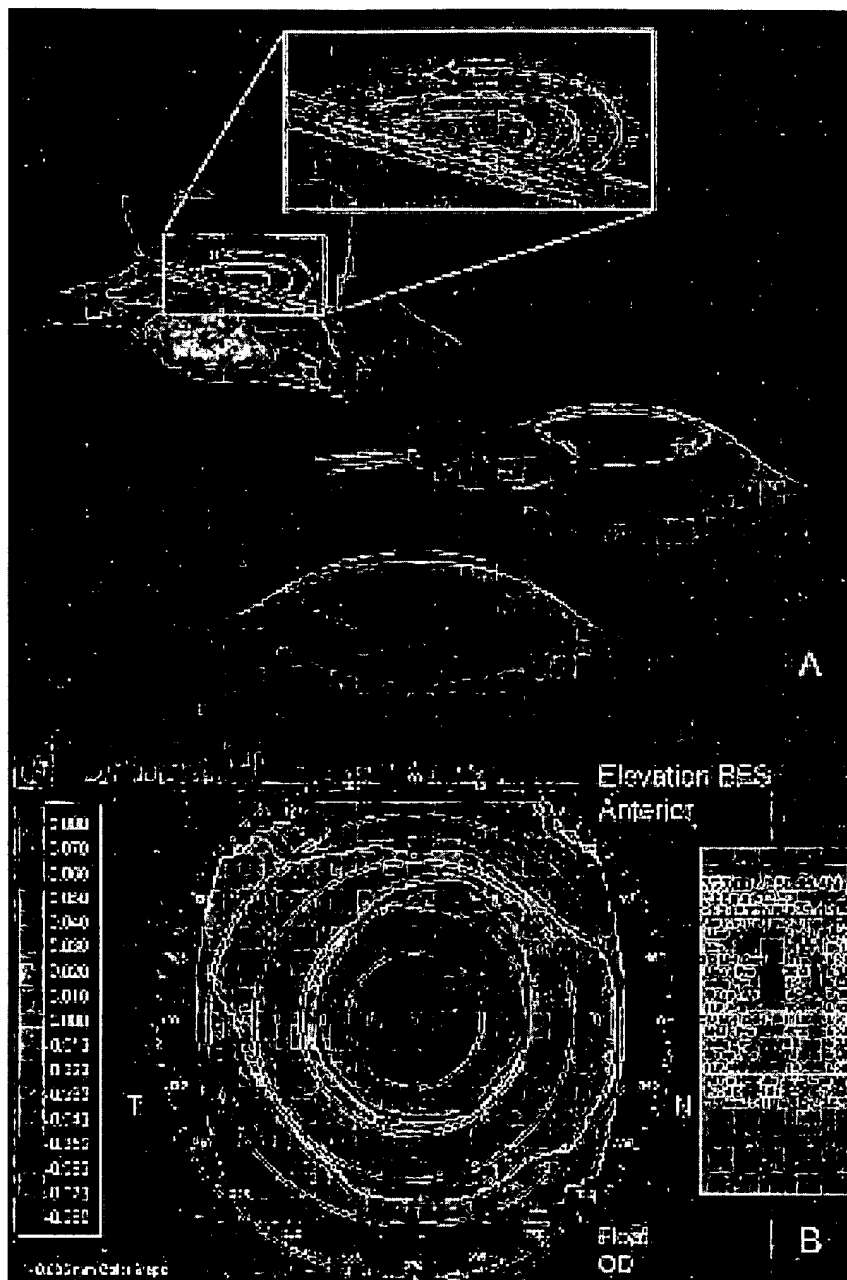


Figure 9. **A)** Conceptual illustration of femtosecond laser keratomileusis (courtesy IntraLase Corporation, Irvine, CA), and **B)** corneal elevation topography (Orbscan) at 3 months after femtosecond laser keratomileusis reveals improvement of about 10 diopters.

the removal of an intrastromal lenticule, resulting in a refractive change analogous to current LASIK techniques. Compared to LASIK, femtosecond laser keratomileusis is a single-step procedure. It is performed on a low vacuum fixated eye, which makes centration both accurate and easy to maintain. For clinical use of femtosecond laser keratomileusis, a surgical nomogram describing the shape, size, and position of the lenticule has been designed on the basis of an accurate analytical model of the human cornea.¹⁸ The accuracy, reproducibility, stability, and

safety of this procedure must be determined in a larger series of patients.

Femtosecond laser intrastromal photorefractive keratectomy is a new method for correcting low myopia and hyperopia without any cuts on the corneal surface. The epithelium and Bowman's layer remain intact, hence patients do not have pain or discomfort following the procedure. Since the refractive results are of significant magnitude and remain stable, resulting in excellent patient satisfaction, this treatment has a promising future after clinical

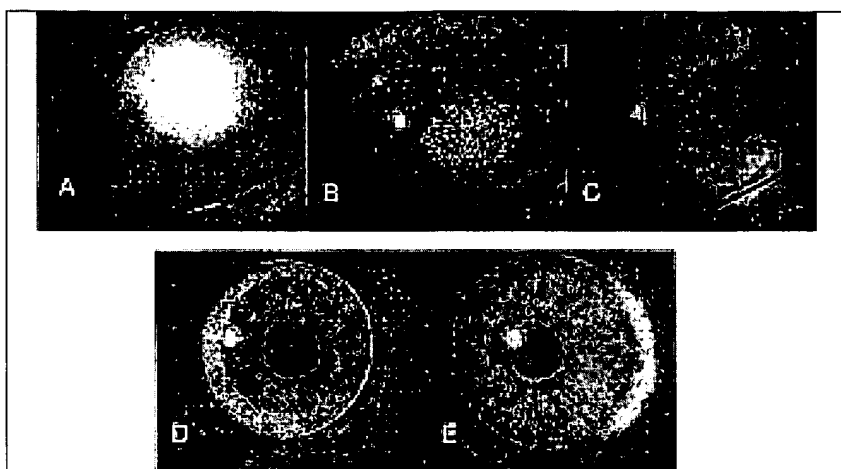


Figure 10. Slit-lamp photomicrographs after intrastromal photorefractive keratectomy for myopia: A) immediately after surgery, B) after 1 hour, and C) after 1.5 hours; D) immediately after intrastromal photorefractive keratectomy for hyperopia; and E) one-half hour after intrastromal photorefractive keratectomy for hyperopia.

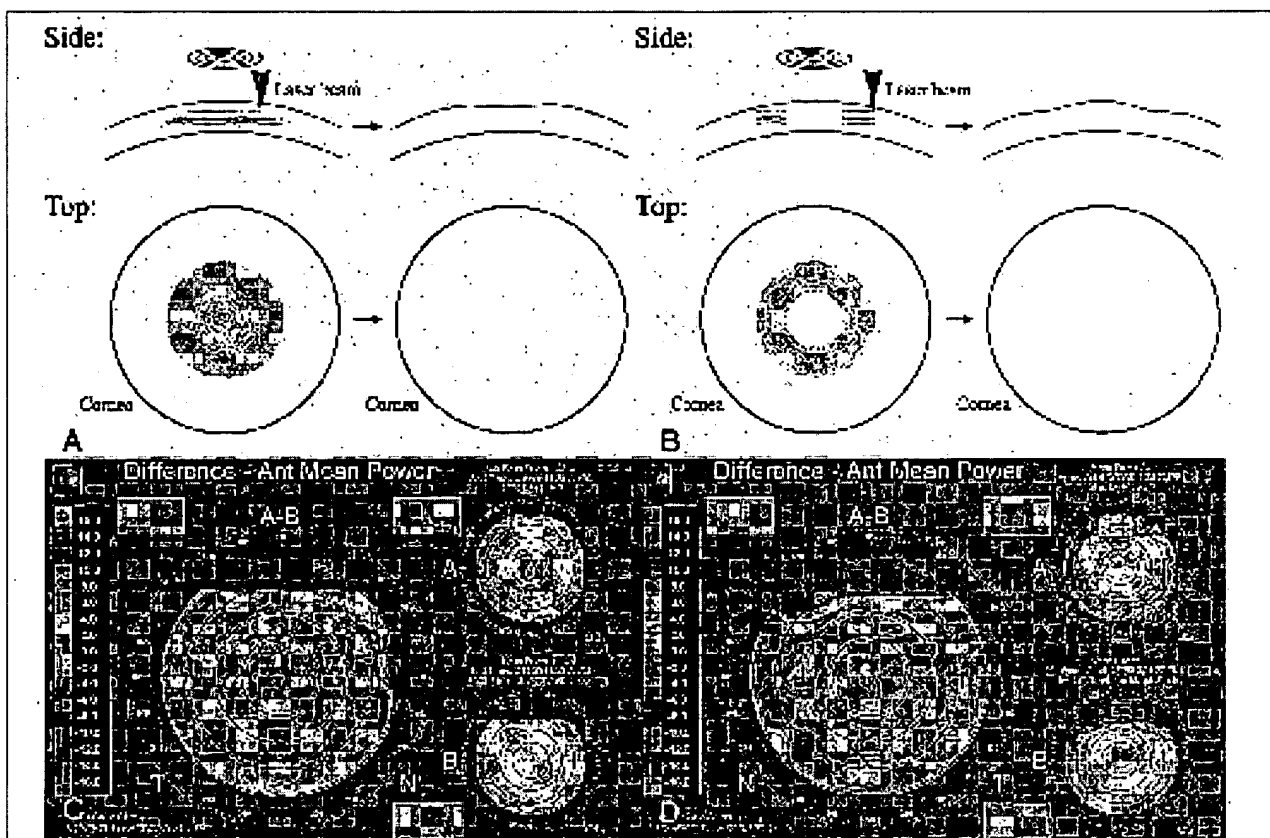


Figure 11. Diagram of pulse placement for volume reduction with intrastromal photorefractive keratectomy: A) for myopia, and B) for hyperopia. Six-month postoperative corneal topography of intrastromal photorefractive keratectomy C) for myopia, and D) for hyperopia. Corneal topography demonstrates an approximate 3.00-D change for each condition.

validation in a large number of patients. The 3.00 D of myopic (or hyperopic) change corresponds to 7 to 10 layers of pulses, which remove a depth of 3 to 5 μm each, resulting in a maximum central (or peripheral) depth of 20 to 50 μm . The mean of this

range corresponds to the depth of 3.00 D with conventional laser vision correction.

The potential advantages of the femtosecond laser keratome include the ability to vary multiple parameters, maintain normal intraocular pressure,

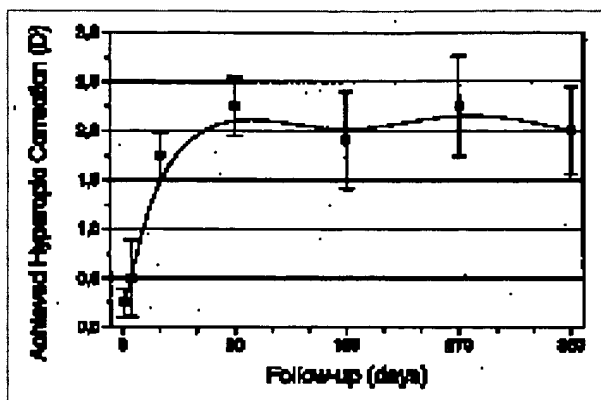


Figure 12. Average achieved hyperopic correction during follow-up after ISPRK in nine eyes.

and increase postoperative stability of the flap. Femtosecond lasers may also have significant potential for improving corneal transplantation (anterior, or posterior lamellar and full-thickness transplantation), as well as surgical manipulation of other ocular tissues, such as the sclera (glaucoma surgery) and the lens (cataract surgery or presbyopia correction). Continuous improvements in ultrafast laser technology and the increasing demands from ophthalmologists to improve available surgical techniques suggest that the femtosecond laser in refractive surgery will evoke further investigation.

REFERENCES

1. Spooner GJR, Juhasz T, Ratkay-Traub I, Djotyan G, Horvath C, Sacks Z, Marre G, Miller D, Williams AR, Kurtz R. New development in ophthalmic applications of ultrafast lasers. Commercial and Biomedical Applications of Ultrafast Lasers II, Proceedings of SPIE 2000;3934:62-72.
2. Juhasz T, Djotyan G, Loesel FH, Kurtz RM, Horvath C, Bille JF, Mourou G. Applications of femtosecond lasers in corneal surgery. *Laser Physics* 2000;10:1-6.
3. Puliafito CA, Steinert RF, Deutsch TF. Excimer laser ablation of the cornea and lens. *Ophthalmology* 1985;92:741-748.
4. Vogel A, Capon MRC, Asiy-Vogel MN, Birngruber R. Intracocular photodisruption with picosecond and nanosecond laser pulses: tissue effects in cornea, lens, and retina. *Invest Ophthalmol Vis Sci* 1994;35:3032-3044.
5. Juhasz T, Kastis GA, Suárez C, Bor Z, Bron WE. Time-resolved observations of shock waves and cavitation bubbles generated by femtosecond laser pulses in corneal tissue and water. *Lasers Surg Med* 1996;19:23-31.
6. Krueger RR, Marchi V, Gualano A, Juhasz T, Speaker M, Suárez C. Clinical analysis of the Nd:YLF picosecond laser as a microkeratome for laser in situ keratomileusis. *J Cataract Refract Surg* 1998;24:1-7.
7. Kurtz RM, Liu X, Elner VM, Squier JF, Du D, Mourou GA. Photodisruption in the human cornea as a function of laser pulse width. *J Refract Surg* 1997;13:643-658.
8. Kurtz RM, Horvath C, Liu HH, Krueger R, Juhasz T. Lamellar refractive surgery with scanned picosecond and femtosecond laser pulses. *J Refract Surg* 1998;14:541-548.
9. Yen KG, Sachs Z, Elner VE, Traub IR, Juhasz T, Kurtz RM. Histopathology of femtosecond laser intrastromal refractive surgery in rabbits [abstract]. *Invest Ophthalmol Vis Sci* 1999;40(suppl)621.
10. Pallikaris IG, Papatzanaki ME, Siganos DS, Tsilimbaris MK. Corneal flap technique for laser in situ keratomileusis: human studies. *Arch Ophthalmol* 1991;109:1699-1702.
11. Pallikaris IG, Siganos DS. Laser in situ keratomileusis to treat myopia: early experience. *J Cataract Refract Surg* 1997;23:39-49.
12. Binder PS, Moore M, Lambert RW, Seagrist DM. Comparison of two microkeratome systems. *J Refract Surg* 1997;13:142-153.
13. Buratto L, Ferrari M, Rama P. Excimer laser intrastromal keratomileusis. *Am J Ophthalmol* 1992;113:291-295.
14. Knorz MC, Liermann A, Seiberth V, Steiner H, Wiesinger B. Laser in situ keratomileusis to correct myopia from -6.00 to -29.00 diopters. *J Refract Surg* 1996;12:575-584.
15. Seiler T, Kousala K, Richter G. Iatrogenic keratectasia after laser in situ keratomileusis. *J Refract Surg* 1998;14: 312-317.
16. Alio JL, Perez-Santonja JJ, Tervo T, Tabbara KF, Vesaluoma M, Smith RJ, Maddox B, Maloney RK. Postoperative inflammation, microbial complications, and wound healing following laser in situ keratomileusis. *J Refract Surg* 2000;16: 523-538.
17. Schanzlin DJ, Abbott RL, Asbell PA, Assil KK, Burris TE, Durrie DS, Fouraker BD, Lindstrom RL, McDonald II JE, Verity SM, Waring III GO. Two-year outcomes of intrastromal corneal ring segments for the correction of myopia. *Ophthalmology* 2001;108:1688-1694.
18. Djotyan GP, Kurtz RM, Fernandez DC, Juhasz T. An analytically solvable model for biomechanical response of the cornea to refractive surgery. *J Biomech Eng-T ASME* 2001;123:440-445.
19. Juhasz T, Loesel F, Kurtz RM, Horvath C, Mourou G. Femtosecond laser refractive corneal surgery. *IEEE Journal of Special Topics in Quantum Electronics* 1999;5:902-910.
20. Ratkay-Traub I, Juhasz T, Horvath C, Suárez C, Kiss K, Ferincz I, Kurtz R. Ultra-short pulse (femtosecond) laser surgery: Initial use in LASIK flap creation. *Ophthalmol Clin N Am* 2001;14:347-355.
21. Vogel A, Hentschel W, Holzfuss J, Lauterborn W. Cavitation bubble dynamics and acoustic transient generation in ocular surgery with pulsed neodymium:YAG laser. *Ophthalmology* 1986;93:1259-1269.

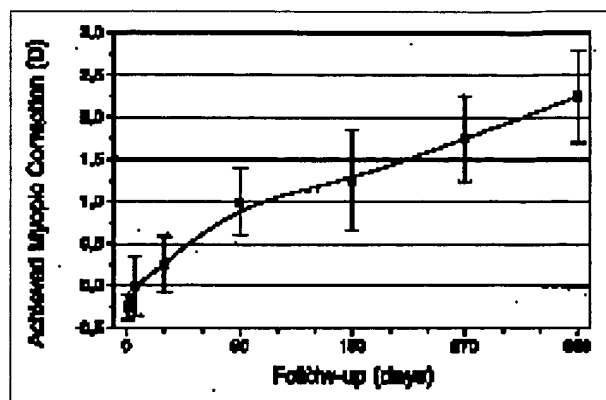


Figure 13. Average achieved myopic correction during follow-up after ISPRK in four eyes.